Heterostructures of 2D TMDs and BN

A Thesis

Submitted in partial fulfillment of the degree of

Master of Science

as a part of Integrated Ph.D. programme in

Materials Science

by

Rajendra Singh

CHEMISTRY AND PHYSICS OF MATERIALS UNIT

JAWAHARLAL NEHRU CENTRE FOR ADVANCED SCIENTIFIC RESEARCH

Bengaluru-560064, INDIA

April 2018

Dedicated to

My family

DECLARATION

I hereby declare that the thesis entitled "**Heterostructures of 2D TMDs and BN**" is an authentic record of research work carried out by me at the Chemistry and Physics of Materials Unit (CPMU), Jawaharlal Nehru Centre for Advanced Scientific Research, Bangalore, India under the supervision of Professor Dr. Ranjan Datta and that it has not been submitted elsewhere for the award of any degree or diploma.

In keeping with the general practice in reporting scientific observations, due acknowledgment has been made whenever the work described is based on the findings of other investigators. Any omission that might have occurred due to oversight or error in judgment is regretted.

Rajendra Singh

CERTIFICATE

Certified that the work described in this thesis titled "**Heterostructures of 2D TMDs and BN**" has been carried out by **Mr. Rajendra Singh** at the Chemistry and Physics of Materials Unit (CPMU), Jawaharlal Nehru Centre for Advanced Scientific Research, Bangalore, India under my supervision and that it has not been submitted elsewhere for the award of any degree or diploma.

Dr. Ranjan Datta

(Research Supervisor)

Acknowledgements

I take this opportunity to sincerely thank my research supervisor Prof. Ranjan Datta for his constant motivation, excellent guidance, encouragement and advice he has provided throughout my M.S. I have been extremely lucky to have a supervisor who cared so much about my work, and who responded to my questions and queries so promptly. I remain amazed that despite his busy schedule, he was able to go through the final draft of my M.S. thesis and respond my every mail in less than an hour with comments and suggestions on almost every page. He is an inspiration. His valuable instructions, comments and suggestions in preparing research manuscripts have helped me immensely. His endless enthusiasm for science and hard working nature has inspired and motivated me at various times.

I sincerely thank Bharat Ratna Prof. C. N. R. Rao for creating world class facilities at International Centre for Materials Science (ICMS). I specially thank him for providing aberration corrected transmission electron microscope facility and pulsed laser deposition crystal growth facility at this centre which gave me an excellent opportunity to learn and carry out research.

I thank the past and present chairman of Chemistry and Physics of Materials Unit, Prof. S. Balasubramanian and Prof. Chandrabhas Narayana for all their invaluable support. I would like to take this opportunity to specially thank all the professors who offered me courses on various subjects, starting from Prof. S. Balasubramanian, Prof. N. S. Vidyadhiraja, Prof. S. K. Pati, Prof. K. S. Narayan, Prof. T. K. Maji, Prof. A. Sundaresan, Prof. S. Easwaramoorthy, Prof. N. Chandrabhas, Prof. U.V. Waghmare, Prof. Shobhana Narasimhan, Prof. M. K. Prakash and Prof. R. Datta. for their excellent teaching and the courses they have offered.

I would like to thank the entire faculty at JNCASR for being a constant source of inspiration with their advanced research. I take this opportunity to thank all my past teachers

at school and college level for sharing their knowledge, providing their support and encouragement without which it is impossible for me to be here. I take this opportunity to thank my past and present labmates, Dr. Loukya, Dr. Devendra Singh Negi, Dr. Rajib Sahu, Mr. Badri Vishal, Ms. Usha Bhat, Ms. Sharona Horta, Ms. Shallu Rani and Mr. Ankit Sharma for their useful discussions and creating a cheerful environment.

I extend my gratitude to all the efficient staff at the Library, Academic and Administration sections for their timely help and cooperation.

I acknowledge and thank all my friends from the integrated PhD 2015 batch – Sukanya Das (for your kind heart and supporting me every time), Janaky S. (tension free girl), Lakshay Dheer (my best roomate ever), Narendra Kumar (making me laugh at every meeting) and Niloyendu Roy (for offering me .....on the first day of JNC).

I also thank all the friends I made in JNCASR while at recreation and sports, Manjeet, Rajendra, Pawan, Aurbinda, Nimish, abhijeet, to name a few.

I also thank all the friends I made outside of JNCASR Avinash, Harish, Rajesh, Pritam, Subham, Amit, Neeraj kumar, Neeraj choudhary, Sandhya, Praveen, Akshay kumari, Vijaypal, Surendra rathor, Darasingh.....

I finally acknowledge and thank all my parents and family members for their unconditional love, support and encouragement. From my heart I acknowledge to my sister Suman.

Preface

This thesis entitled “Heterostructure of TMDs and BN” has been divided into 5 chapters.

Chapter 1 gives the introduction of 2D materials and van der Waals heterostructures.

Chapter 2 describes the epitaxial growth technique (PLD), synthesis of lateral and vertical van der Waals heterostructure by sintering and liquid exfoliation technique and characterization techniques.

Chapter 3 describes experimental procedures and synthesized lateral and vertical van der Waals heterostructures of TMDs and BN.

Chapter 4 Growth of w-BN thin film by PLD and electronic properties of BN bilayer in different rotational stacking faults.

Chapter 5 deals with the conclusion of the experimental results and future prospects.

Contents

List of figures:

Figure 4.3 Atomic structure of h-BN layers in AA' stacking. (a) HRTEM image of h-BN layes. (b) HRTEM image is low-pass filtered HRTEM image, no artifacts are caused to remove noise in HRTEM images. The filtering is low-pass and used to remove noise and increase visibility of HRTEM images. (c) 2D fast Fourier transform (FFT) of h-BN HRTEM image. Six spots adjacent to the center are {1-100}.

Figure 4.4 Atomic structure of h-BN layers in AB stacking and comparing with theoretical structure. (a) HRTEM image of h-BN in AB stacking. (I) Magnified HRTEM image of (a). (II) the lattice constant in direction of the small red arrow. (III) Lattice constant along the big red arrow. (IV) Atomic structure model in AB stacking showing all the lattice parameters is matching with HRTEM image.

Figure 4.5 HRTEM images and FFT patterns of a bilayer h-BN sheet with 30^{o} of ratational stacking.This HRTEM image is raw and unfiltered. the twelve $\{11\bar{0}0\}$ spots constitute two hexagons that are indicated with red and yellow hexagon.

Figure 4.6 HRTEM images and FFT patterns a few layers h-BN nanosheet with three rotational stacking faults. (a),(b) and (c) are FFT pattern from selected region of interest I, II and III respectively. (d) is FFT pattern of whole HRTEM.

Figure 4.7 (a) & (b) HRTEM image of *w*-BN on c-plane sapphire along two different zone axes of sapphire showing atomic arrangement and registry of atoms at the film substrate interface. The inter-atomic distances are mentioned in the figure.

Figure 4.8 Schematic structure of monolayer (a) staggered h-BN on c-plane sapphire. The stability of staggered h-BN configuration is 210 meV/atom more compared to flat h-BN. (b) staggered bilayer h-BN showing nucleation and growth of w-BN phase along c direction. Charge density plot showing additional interaction between B and O atoms at the interface in both (c) mono and (d) bi-layer leading to staggering configuration of flat h-BN.

List of Tables:

Chapter-I

2D Materials

1.1 Introduction

The journey of 2D materials when successful isolation of monolayer graphene from bulk graphite was demonstrated by A.K. Geim et al [1]. 2D materials provide the thinnest platform to make ultrathin electronic devices beyond Moore's law [2]. In graphene, carbon atoms are covalently bonded in a honeycomb lattice and is the basic building block of other important carbon structure such as graphite, fullerene and carbon nanotube. In this 2D honeycomb structure graphene has amazing physics and various extraordinary properties such as massless Dirac fermions[4], distinctive integer and half-integer quantum Hall effect [4-6], Klein Tunneling [7-8], ultra-high electron mobility (200,000 cm−2V−1s−1) [9-11] , very high thermal conductivity (600Wm-1K-1)[12] , high intrinsic strength and Young's modulus [13], very high surface area and ~ 97% transmittance for IR-UV range [14-15]. All these properties benefits graphene in many application including: ballistic transport [65], solar cell [16], energy storage [17], biosensors [18] , wearable device[19], transparent electrodes [20] and catalysis[21]. Although graphene has all these extraordinary properties but pristine graphene does not have band gap and cannot be used in the application where band gap is required. The lack of a semiconducting band gap in graphene, devices made from graphene is difficult to switch off and losing the advantage of graphene's high electrical conductivity and low static power consumption. To overcome this band gap problem, many theoretical and experimental studies have been done on graphene to open a small band gap. Chemical substitutional doping is one way by which both n, as well as p-type doping, can be achieved by substituting carbon with nitrogen [22-31], boron [23, 26-28,32-35] or both [36-37].

Strain-induced band gap opening [38], by forming other structures such as graphene nanoribbons opens up band gap [39-41] and by constructing van der-Waals heterostructure with h-BN and TMDs [42]. Nevertheless, none of the methods is sufficient to provide enough high on-off current ratio while retaining the advantage of the graphene's ultrahigh mobility.At

the same time,22 there are many other 2D materials, they are semiconductor in nature gave the birth to research on these 2D materials. Therefore, research is being directed toward new 2D materials. These include 2D TMDs (e.g. molybdenum disulfide (MoS2), molybdenum diselenide (MoSe2), tungsten disulfide (WS2), and tungsten diselenide (WSe2), hexagonal boron nitride (h-BN), rhenium disulfide (ReS2)) [43-45] etc.

Most TMDs in bulk form is indirect band-gap semiconductors, whereas their monolayer has direct bandgaps [46], which is favorable for optoelectronic applications. The bulk MoS2, an indirect-gap semiconductor with a band gap of 1.29 eV [47] whereas monolayer MoS2 is a direct bandgap of 1.9 eV[48], this existence of the native bandgap provides an excellent current on/

off ratio of [$1x10^8$] in single-layer MoS2 based field-effect transistors [49].

This property of MoS2 is inspiring, which will largely compensate the weakness of gapless graphene, thus making it possible for 2D materials to be used in the next generation electronic devices.

1.2 Van der Waals heterostructure

Stacking of two or more different semiconducting materials, on top of each other is commonly referred to as heterostructure. Such a stack can be performed by mechanical assembly or by crystal growth techniques. The difference between difference semiconducting layers permits spatial confinement of injected charge carriers, electron and hole. Based on the energy band alignments, heterostructures can be divided into three categories, i.e. type-I (symmetric), type-II (staggered) and type -III (broken). Most of the TMDs form either type-I or type-II heterostructure [66]. Type -II and type -III heterostructure have same properties so only type-I and type-II heterostructures have been studied extensively.

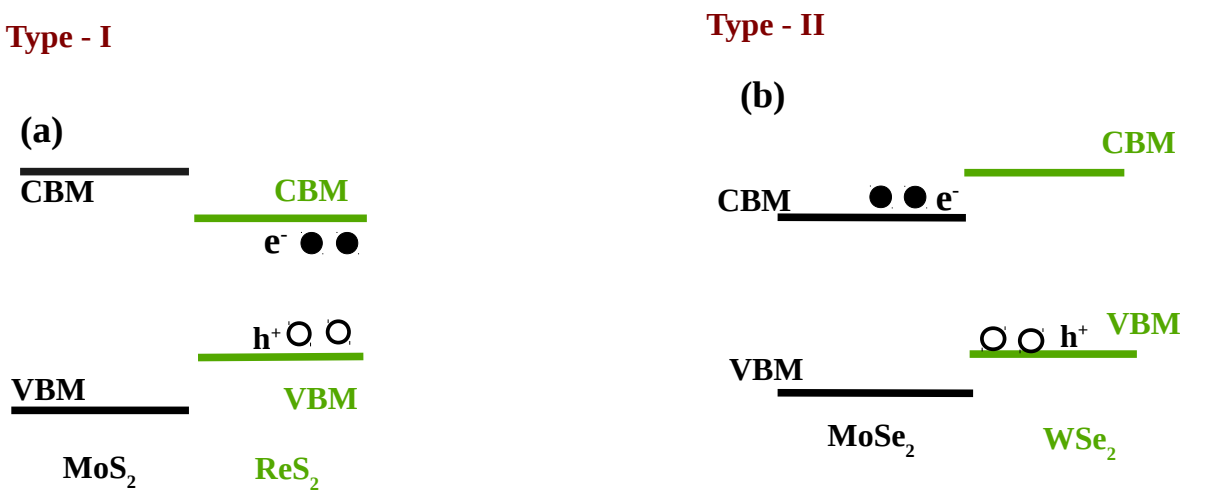

Figure. 1.1 Schematic of the band alignment between two semiconductors, showing type-I (a) and type-II (b) alignments.

Type-I heterostructure

From figure 1.2 (a) in type -I heterostructure both the conduction band minimum (CBM) and the valence band maximum (VBM) are located in the material with the smaller bandgap. If we take MoS_2 and ReS_2 as an example they form type I heterostructure [50]. When electrons and holes are excited in the wide-gap material (MoS_2) then transfer to the small-gap material (ReS_2) because electrons go to lower energy level and holes go to higher energy level. This spatial confinement of electrons and holes in the same region facilitates their radiative recombination. This ability of type -I heterostructure widely utilized in optical devices, like light emitting diodes (LEDs) and laser [51]. Carriers excited in the smaller-gap material (ReS_2) are prohibited from interlayer transfer due to their lower energies.

Light emitting diodes (LEDs) based on type I heterostructures with transition metal dichalcogenides (TMDs) sandwiched between h-BN and graphene has been engineered [52].

Type – II heterostructure

In type II heterostructure conduction band (CB) and valence band (VB) are located in different materials. If we take $MoSe_2$ WSe_2 as an example they form type II heterostructure.

Where conduction band is located in $MoSe_2$ whereas valence band in WSe_2. When electron and holes are excited in $MoSe_2$ holes go to WSe_2 layer and electron remains in the same layer. This is useful for solar cell application where electron and holes separation is required. In this heterostructure electrons and holes reside on different layers of semiconductor that prevent them to recombine easily and increases their lifetime. Type II heterostructure using graphene/TMDs/graphene has recently been demonstrated to exhibit to fast charge carriers separation in photovoltaic device [53]. Type -II heterostructure based on MoS_2/WS_2 [54-55], WSe_2/WS_2 [56], MoS_2/WSe_2 [57], $WSe_2/MoSe_2$ [58], Graphene/WSe_2/MoS_2/Graphene [59], p-MoS_2/n-MoS_2 [60], p-WSe_2/n-WSe_2 [61], have been reported.

Two-dimensional van der Waals materials (MoS_2, WS_2, h-BN) have strong in-plane covalent bond whereas weak van der Waals interaction in out of the plane. The weak van der Waals forces that allow exfoliation of these bulk materials into single layers. These layers are free of dangling bonds in c-direction. This gives an opportunity to assemble different 2D material on top of each other in the desired order to create van der Waals heterostructures [68]. The resulting van der Waals heterostructures not only combine the individual properties of the layers that they have, but they also present new physical effects and interesting possibilities for engineering their optoelectronic properties like Massive Dirac Fermions and Hofstadter Butterfly [67]. The lack of lattice matching constraints introduces several degrees of freedom to form these heterostructures, such as the thickness of the layers, their sequence, and their rotational alignment. There are two ways of constructing heterostructure, based on stacking procedures heterostructure can be divided into two parts: vertical heterostructure and lateral heterostructure.

1.2.1 Vertical van der Waals heterostructure

In verticle heterostructure, different layers of 2D materials are stacked layer by layer on top of each other. There are no constraints of lattice mismatch to form verticle heterostructure because there is no chemical bond happening in c-direction.

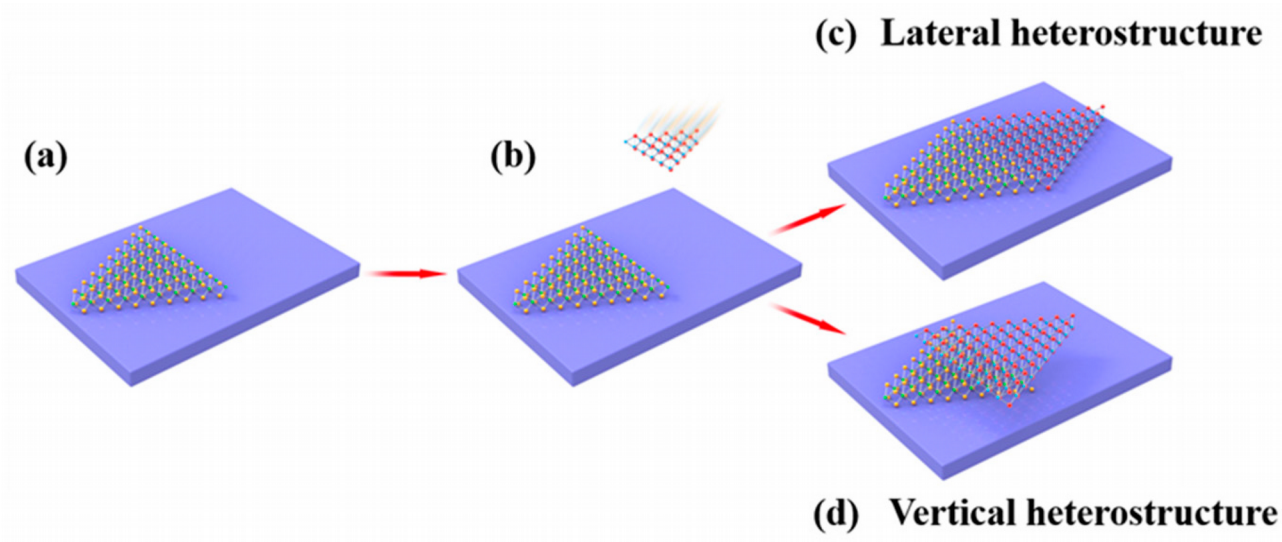

Figure 1.2 Schematic of the preparation of verticle heterostructure. (a) First growth of the 2D material on the substrate. (b) Growing second material with the first layer of 2D material to construct heterostructure. (c) Formation of the lateral heterostructure. (d) Formation of the vertical heterostructure.[74]

From Figure 1.2(a) we can see that first one layer of 2D material is synthesized on a substrate. Next procedure is the key step that decides weather heterostructure will be verticle or lateral. In this step layer of second material is growing or transferring to the first layer, If this layer is stacking onto the first layer, then it will be vertical heterostructure.

1.2.2 Lateral van der Waals heterostructure

The lateral (in-plane) heterostructure, which can be obtained by stitching two layers of 2D materials into a shared platform with a one-dimensional (1D) interface. Layered 2D materials have no dangling bond in c-direction but have the dangling bond in-plane direction. By activating these dangling bonds we can stitch them to form the lateral heterostructure. The lateral heterostructure is usually connected by covalent bonds so lattice constant of two materials should be comparable to each other. Covalent bonds ensuring the epitaxial quality thus improving optical and electrical properties of the heterostructure.

From (figure 3) first grown and second materials are connected in-plane, they form lateral heterostructures.

1.3 Growth techniques for van der Waals heterostructure

There is various type of synthesis method on van der Waals heterostructures. Liquid exfoliation techniques (ion intercalation and ultrasonication) and chemical vapor deposition (CVD) are the most used technique.

1.3.1 Liquid exfoliation technique (ion intercalatioin and ultrasonication)

Liquid exfoliation by applying sound energy and ion intercalation can produce large volumes of dispersed monolayers and few-layer flakes of various 2D materials, cheaply and with the potential for scale-up. These liquid-based exfoliation techniques allow the easy creation of thin films.[69]

1.3.2 Pulsed Laser Deposition (PLD)

Pulsed laser deposition (PLD) is a fast and simple thin film growth technique in which a low wavelength photon energy of a laser characterized by pulse duration (ns-fs) and laser frequency interacts with a bulk material. This produces instant local vaporization at the

surface of the target material and generates a plasma plume. Plasma plume contains photons, ions, electrons, neutral atoms, molecules and chunks of the target material. This plasma plume is collected on the hot substrate and condense in the form of thin film.[62,70]

1.3.3 Mechanical Exfoliation Method

In mechanical exfoliation, a scotch tape is used to produce the thin film of 2D materials. 2D materials have weak van der Waals interaction between layers, so can easily come out in a monolayer with scotch tape. These layers can be transferred to a different substrate such as Al_2O_3, SiO_2 etc. Then one monolayer of different materials precisely transferred onto the first layer to form vertical heterostructure [71].

1.3.4 Chemical Vapor Deposition (CVD)

chemical vapor deposition (CVD) is one of the most promising technique to grow both vertical and lateral van der Waals heterostructure of various TMDs. It can create large area high-quality thin film of 2D materials on a substrate with a well-controlled lateral size and layer thickness, which is well suited for device fabrications. First WS_2–MoS_2 lateral and vertical heterostructure has been grown by one-step CVD [72]

1.3.5 Molecular Beam Epitaxy (MBE)

Many heterostructures of TMDs has grown using molecular beam epitaxy. It requires ultra-high vacuum. Heterostructures of 2D TMDs and insulating h-BN has been grown [73].

1.3.6 Physical Vapor Transport/Deposition (PVT/PVD)

Physica vapor deposition is simple technique to deposite thin film. This technique consists three fundamental steps: First is vaporization of a material from solid source, secon step is

transportation fo vapor to the substrate and third step is condensation of vapor on a substrate to grow thin film. There are reports to grow thin film of TMDs using PVD technique [76]

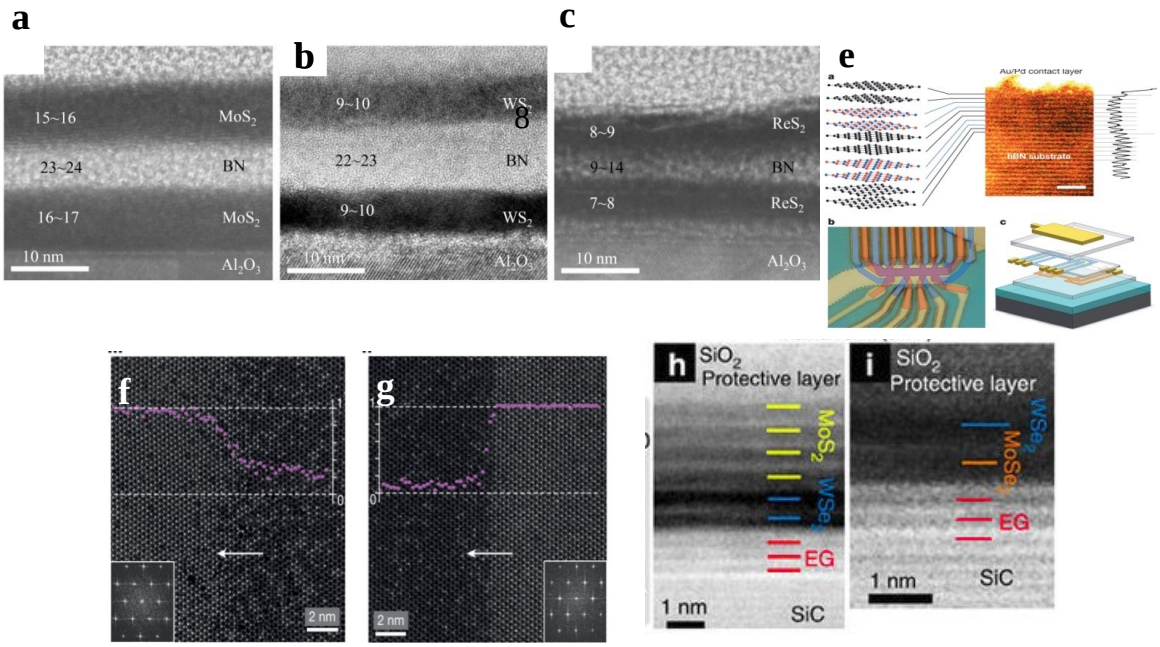

Figure 1.3 Lateral and vertical van der Waals heterostructure are grown by various growth techniques. (a), (b), (c) vertical heterostructure of different TMDs with h-BN by pulsed laser deposition (PLD) (in our lab) [62]. (e) The vertical heterostructure of graphene and h-BN by mechanical exfoliation [75] (f),(g) lateral heterostructure of $MoSe_2$-WSe_2 by chemical vapor deposition (CVD) [63]. (h), (i) Vertical heterostructure of MoS_2-WSe_2 and WSe_2-$MoSe_2$ by metal-organic chemical vapour deposition (MOCVD) [64].

Bibliography:

[1] K. S. Novoselov, et al., Science 2004, 306, 666.

[2] G. E. Moore, Proc. IEEE 86, 82 (1998).

[3] Geim AK, et al., Physics Today 2007;60(8):35–41.

[4] K. S. Novoselov, et al., Nature, 2015, 438.

[5] C. R. Dean, et al., Nature Phys. 7: 693–696, 2011.

[6] Novoselov KS et al., Science 315: 1379, 2007.

[7] Zalipaev VV, et al., Phys. Lett. A 377: 216–221, 2013.

[8] Kusmartsev F.V., Wu W.M., Pierpoint M.P., Yung K.C. (2015). Progress in Optical Science and Photonics, vol 2. Springer, Singapore.

[9] Neto AHC and Novoselov KS, Rep. Prog. Phys. 74: 082501, 2011.

[10] Schwierz F., Graphene transistors, Nature Technology 5, 487–496, 2010.

[11] Kusmartsev FV et al., JETP Lett. 42: 257–260, 1985.

[12] Prasher R. Graphene spreads the heat. Science 328: 185–186, 2010.

[13] C. Lee, X. D. Wei, J. W. Kysar and J. Hone, Science 321 (5887), 385 (2008)

[14] M. D. Stoller, et al., Nano Lett 8 (10), 3498 (2008).

[15] Bonaccorso F, et al., Nature Photonics 4: 611–622, 2010.

[16] H. Wang, et al. Angew. Chem. Int. Ed. 52 (2013) 9210.

[17] C. Liu, et al. Nano Lett. 10 (2010) 4863.

[18] https://doi.org/10.1016/j.snb.2013.06.045

[19] Wang Y, et al., Adv Funct Mater 2014;24:4666e70.

[20] Bae S, Kim H, et al.. Nat Nanotechnol 2010;5:574e8.

[21] Lonkar SP, et al., J Thermodyn Catal 5:132. doi: 10.4172/2157-7544.1000132.

[22] D. Wei et. al. Nano Letters 9 (5), 1752 (2009).

[23] L. S. Panchakarla et. al., Advanced Materials 21 (46), 4726 (2009).

[24] S. S. Yu, W. T. Zheng, Q. B. Wen and Q. Jiang, Carbon 46 (3), 537 (2008).

[25] Y. Li, Z. Zhou, P. Shen and Z. Chen, ACS Nano 3 (7), 1952 (2009).

[26] A. Lherbier et. al. Physical Review Letters 111, 036808 (2008).

[27] X. H. Zheng et. al. The Journal of Physical Chemistry C 114 (9), 4190 (2010).

[28] R. Peköz et. al. Nanostructures 42 (2), 110 (2009).

[29] Y. Shan Sheng, et. al. IEEE Transactions on 9 (1), 78 (2010).

[30] F. Cervantes‐Sodi et al. Physical Review B 77, 165427 (2008).

[31] N. Li, et al. Carbon 48 (1), 255 (2010).

[32] X. Ma et al. Carbon 35 (10‐ 11), 1517 (1997).

[33] S. Dutta and S. K. Pati, The Journal of Physical Chemistry B 112 (5), 1333 (2008).

[34] T. B. Martins, et al., Physical Review Letters 98, 196803 (2007).

[35] A. Quandt, et al. physica status solidi (b) 245 (10), 2077 (2008).

[36] L. Ci, L. Song, et al., Nat Mater 9 (5), 430 (2010).

[37] J. Li and V. B. Shenoy, Appl Phys Lett 98 (1), 013105 (2011).

[38] T. Kawasaki, Surf. Rev. Lett. 9, 1459 (2002).

[39] K. Nakada, et al., Phys Rev B 54 (24), 17954 (1996).

[40] K. Wakabayashi, et al., Phys Rev B 59 (12), 8271 (1999).

[41] M. Fujita, et al., J. Phys. Soc. Jpn. 65, 1920 (1996).

[42] Doron Naveh and Elias Towe Nano Lett. 2011, 11, 1070–1075.

[43] Q. H. Wang, et al. Nat. Nanotechnol. 7, 699 (2012).

[44] J. A. Wilson, A. D. Yoffe, Adv. Phys. 18, 193 (1969).

[45] D. Golberg*et al*., Boron nitride nanotubes and nanosheets. 4, 2979 (2010).

[46] Gui-Bin Liu, et al. *Chem. Soc. Rev.*, 2015,44, 2643-2663.

[47] Gmelin Handbook of Inorganic and Organometallic Chemistry (Springer-Verlag, Berlin, 1995), 8th ed., Vol. B7.

[48] K. Dileep, et al., JAP, 119, 114309 (2016).

[49] B. Radisavljevic, et al. Nature Nanotechnology,doi:10.1038/nnano.2010.279 (2011).

[50] Matthew Z. Bellus et al. Nanoscale Horiz., 2017, 2, 31–36, 31.

[51] Nakamura et al. Jpn. J. Appl. Phys. 1995, 34, L797.

[52] Rivera, P.; Schaibley, et al. Nat. Commun. 2015, 6.

[53] Britnell, et al. Science 2013, 340, 1311–1314.

[54] Xiaoping Hong, et al. Nat. Nanotechnol. 682-686,9.

[55] Y. Gong, et al. Nat. Mater. 13 (2014) 1135.

[56] X. Duan, et al. Nat. Nanotechnol. 9 (2014) 1024.

[57] M.-Y. Li, et al. Science 349 (6247) (2015) 524.

[58] Y. Gong, et al. Nano Lett. 15 (9) (2015) 6135

[59] C. H. Lee, et al. Nat. Nanotechnol. 9 (9) (2014) 676.

[60] S. Wi, et al. ACS Nano 8 (5) (2014) 5270.

[61] W.J. Yu, et al. Nat. Mater. 12 (3) (2013) 246.

[62] U.Bhat, et al., arXiv:1710.04160 (2017)

[63] Prasan k. Sahoo, et al. *Nature* 553, 63–67 (2018).

[64] Yu-chuan lin, et al., Nat. Commun. 6, 7311 (2015)

[65] Xu Du, et al. Nat. Nanotechnol., **3**, 491–495 (2008).

[66] V. Ongun Ozcelik et al. PHYSICAL REVIEW B 94, 035125 (2016).

[67] B. Hunt, et al. , Science, DOI: 10.1126/science.1237240.

[68]A. Km. Gei, et al., *Nature* 499, 419–425 (2013).

[69] Valeria Nicolosi, et al. Liquid Exfoliation of Layered Materials, SCIENCE, 340 (2013).

[70] Badri Vishal, et al., Superlattices and Microstructures, 115, 197-203, (2018).

[71] Duan, X.D., et al., Chem. Soc. Rev. 2015, 44, 8859–8876.

[72] Gong, Y. Lin, et al., Nat. Mater. 2014, 13, 1135–1142.

[73] Barton, A.T. Yue, et al., Microelectron. Eng. 2015, 147, 306–309.

[74] Haimei Qi , Lina Wang, et al. Crystals 2018, 8, 35; doi:10.3390/cryst8010035.

[75] A.K.Geim, et al., *Nature* 499,419–425,(2013)

[76] Jeong-Gyu Song, Kyunam Park, et al., Appl Microsc 2015;45(3):119-125.

Chapter II

Experimental methods and Characterization techniques

2.1 Pulsed Laser Depositon (PLD)

2.1.1 Introduction

Pulsed laser deposition (PLD) is a thin film growth technique in which a low wavelength photon energy of a laser characterized by pulse duration (ns-fs) and laser frequency interacts with a bulk material. This produces instant local vaporization at the surface of the target material and generates a plasma plume. Plasma plume contains photons, ions, electrons, neutral atoms, molecules and chunks of the target material. This plasma plume is collected on the hot substrate and condense in the form of thin film. Quality of plasma plume depends on factors such as laser power density, pulse duration, absorption and thermal conductivity of target material.

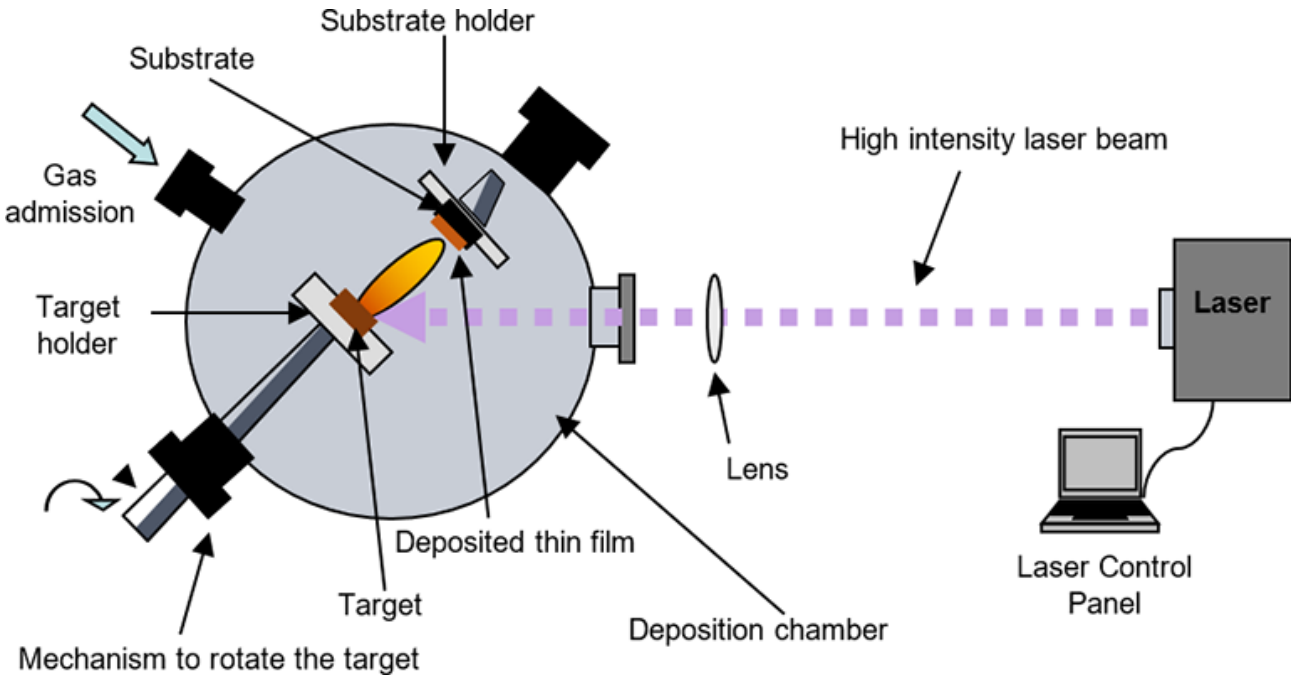

Figure 2.1 Experimental set-up of pulsed laser deposition (PLD) [1]

The principle of PLD is shown in figure 3. A high-intensity laser pulse is focused onto the surface of a target material (solid or liquid) in the deposition chamber and thereby

removes in the form of plasma plume from the target material. This plasma plume is collected on the substrate. Substrate and target have to be placed plane-parallel in the deposition chamber. The removed material is directed towards a substrate where it re-condenses to form a film. Removal of materials occur above a certain threshold power density, and the ejected, partially ionized material forms a luminous ablation plume. For example threshold power for MoS_2 is 15 mJ/cm 2, under 800 nm wavelength irradiation.[2] The threshold power density required to create such a plasma depends on the absorption properties of the target material, the laser wavelength, pulse duration and thermal conductivity of the material. The high-intensity laser source is placed outside the chamber, that is used to irradiate target material and deposit the thin film. Target and substrate are kept in the vacuum chamber and vaporization is induced by the laser beam that is kept outside the vacuum chamber, so no contamination or impurities occurs during growth processes. The growth kinetics of such films depend on the material flux, repetition rate, laser wavelength, target-substrate separation distance, growth temperature, substrate material, pressure, target material (melting point of the target material, thermal conductivity) and background gas (vacuum or reactive gas). The substrate temperature is important to ensure a sufficient surface mobility of the arriving species to support epitaxial growth. Many physical phenomena happen when laser pulse interacts with target material :

1. Coupling of laser beam with the target material.

2. Melting and vaporization of the surface of target material in the form of plasma plume of the thin upper.

3. Photon absorption by vaporized species, which limits further interaction of laser at the target surface.

4. Propagation of plasma plume towards substrate.

5. Return to the initial state after few nanoseconds from the end of the pulse, with a re-solidified surface. [3]

2.1.2 Thin film growth method in PLD

To grow the large area epitaxial thin film of ZnO on highly lattice mismatched (~18%) c-plane sapphire substrate, our group have developed three-step growth process by modifying two-step growth process in PLD. PLD system is much cheaper and fast growth technique than other crystal growth technique like MOCVD, CVD et al. First step is low-temperature nucleation, and second and third step are high-temperature growth. At low-temperature plasma plume (growth initiative particles) have less mobility. Due to less mobility, they can not aggregate to form the large island and this gives complete wetting of substrate. Detailed description about three step growth method is described in reference [4].

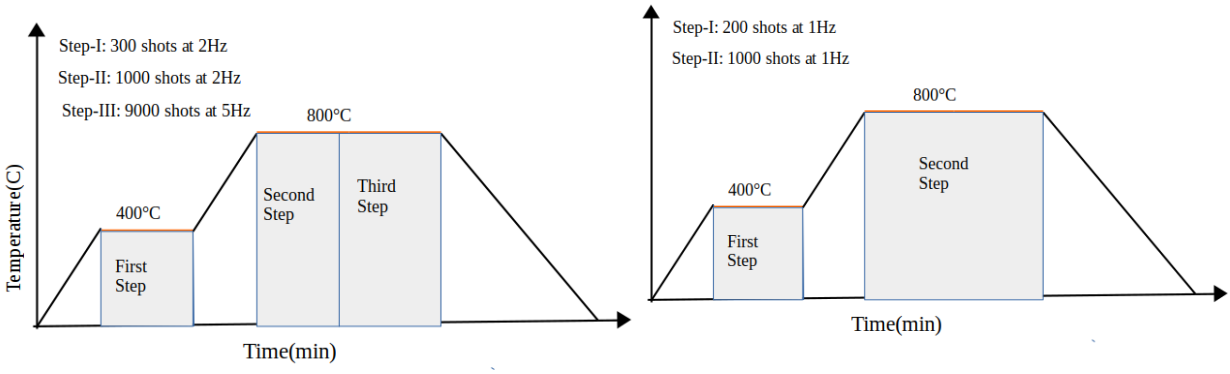

Figure 2.2 (a)Three step growth procedure developed for ZnO growth and (b) two step growth method for TMDs and w-BN

We modified our three-step growth method to two-step growth method with slower kinetics to grow w-BN thin film and van der Waals heterostructures of TMDs on sapphire c-plane. Van der Waals materials do not have the covalent bond in c-direction, there are connected by weak van der Waals force. To grow van der Waals heterostructure we have slow down our growth rate by reducing laser frequency to 1Hz so that materials get enough time to get underlying symmetry. To grow monolayer and multilayer TMDs we have optimized all growth parameters like laser frequency, the number of laser shot, nucleation layer temperature and pressure and final growth temperature [5].

2.2 Sintering

Two-dimensional van der Waals materials (MoS2, WS2, h-BN) have strong in-plane covalent bond whereas weak van der Waals interaction in out of the plane. These materials are free of the dangling bond in the c-direction but have the dangling bond in-plane direction. This is the opportunity to form lateral heterostructures of these 2D materials by activating these dangling bonds, we can stitch them to form the lateral heterostructure. Stitching process can happen by sintering at high temperature. By compacting, neighboring layers of TMDs are held together by cold welds. At sintering temperature, dangling bonds get activation energy and diffusion processes cause necks to form and grow at these contact points to form lateral heterostructures.

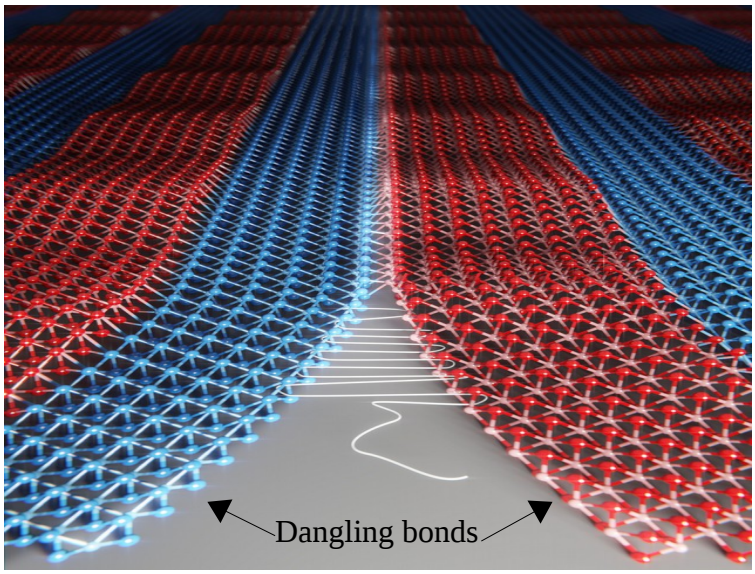

Figure 2.3 Schematic diagram of lateral heterostructure [16].

2.3 Liquid exfoliation by ultrasonication

2.3.1 Introduction

Sonication is a process of applying sound energy to agitate particles dispersed in a solution by converting electrical signals into physical vibration. This is the simplest way to prepare nanoparticle dispersion in liquid solution by applying sound energy. There are two types of sonicator, Bath sonication (indirect sonication) and Probe/horn sonication (direct sonication).

In bath sonication, although the high frequency is used sound waves must transfer to the bath liquid and then it passes through the wall of sample container before reaching the suspension. Whereas in probe sonication probe/horn immersed directly into the solution so there are no barriers to delivering the sound energy to the solution. In that way probe sonication (direct sonication) is more efficient the bath sonication.

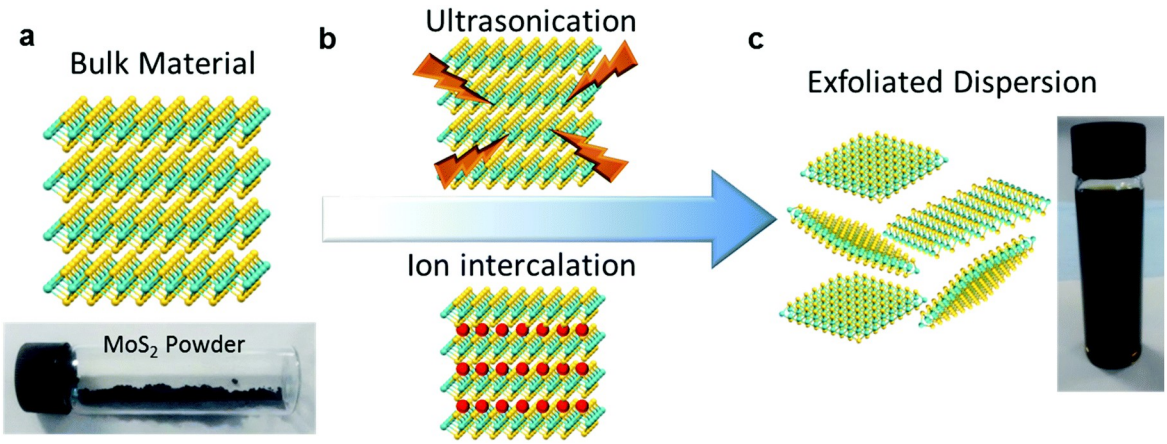

Figure 2.4 Working principle of liquid exfoliation [17] (License Number 4307140299700)

Table 2.1 Specification of sonicator used in this project.

Sonicator tye	Amplitude	Power	Frequency	Tip size	Sample volume
Probe sonicator	20 – 100%	150 – 750 W	20k Hz	3 mm	10 ml

In sonication process ultrasound energy gives sheer force and cavitation acts on the bulk material and exfoliate in nanoparticles. All 2D materials (MoS2, WS2, h-BN) are stacked in the c-direction. The distance between two layers in c-direction is 3-4 Å. These layers are attracted by van der Waals attraction force. This attraction is weak enough to let them separate out in monolayer form but is sufficient enough to hold them together. So it not so easy to exfoliate in monolayers by simple sonication. So our first task is the reduction of the van der Waals force between these layers. To reduce this van der Waals interaction between two adjacent layers we need to depressed bulk powder material in a proper solution. The detailed description of the application of liquid exfoliation by ultrasonication and ion intercalation cab be found in this review[15].

In general liquid exfoliation consist three stapes:

1. Depressed in a liquid (Reduce van der Waals interaction)

2. sonication (Exfoliate in layers)

3. purification (Dry the solvent)

2.3.2 Experiment procedure for liquid exfoliation

For van der Waals heterostructure of TMDs (MoS_2, WS_2) and *h*-BN, we followed a new route that is based on sintering and sonication. This synthesis procedure has three steps.

First step :

In the first step MoS_2, WS_2 and h-BN bulk powder were dispersed in a proper solvent. Proper solvent means material should be dispersed easily and should have a low boiling point so it can vaporize easily. This solution was subjected to ultrasonication at a constant power of 225 W for 7 hours to exfoliate the material in monolayer form. The product formed was in dark color. After sonication, the sonicated solution was kept for 15 hours so that all exfoliated layers of MoS_2, WS_2 and h-BN could settle down on top of each other or side by side to make vertical and in-plane van der Waal heterostructure.

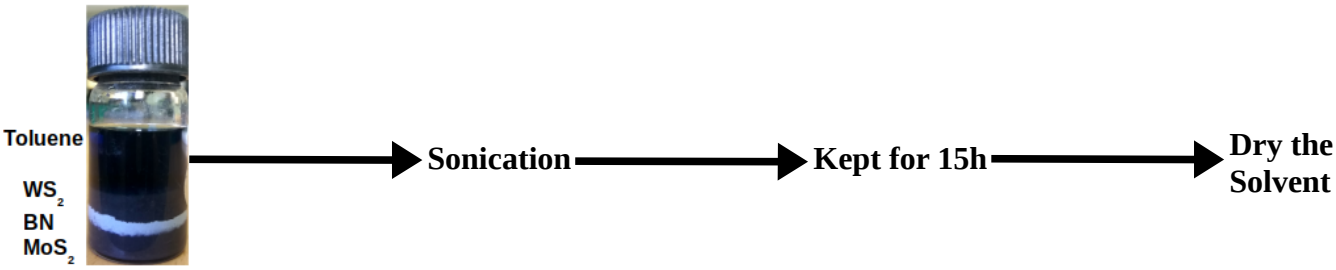

Figure 2.5 Describes the first step of liquid exfoliation.

Second Step :

This step is the sintering process that was most important part of the experiment. We took sonicated dried powder that we got in the first step and using mortar and pestle, a solid pellet was made. Now, this pellet is sintered in the vacuum chamber at 400 °C. The sintering process was followed by Graph 2.1.

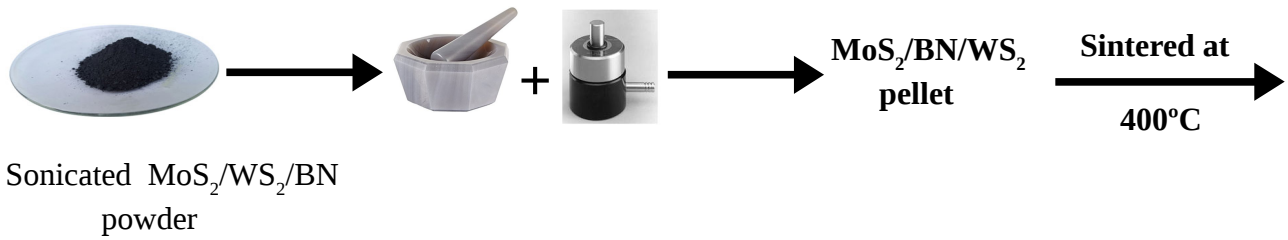

Figure 2.6 The second step of liquid exfoliation, sintering sonicated powder.

Sintering is the most crucial part of the experiment because sintering process decides whether we get MoS_2/WS_2 alloy or MoS_2/WS_2 van der Waals heterostructure. Sintering at high temperature and for a long time end up with alloy formation. So to avoid alloy formation we optimized sintering process.

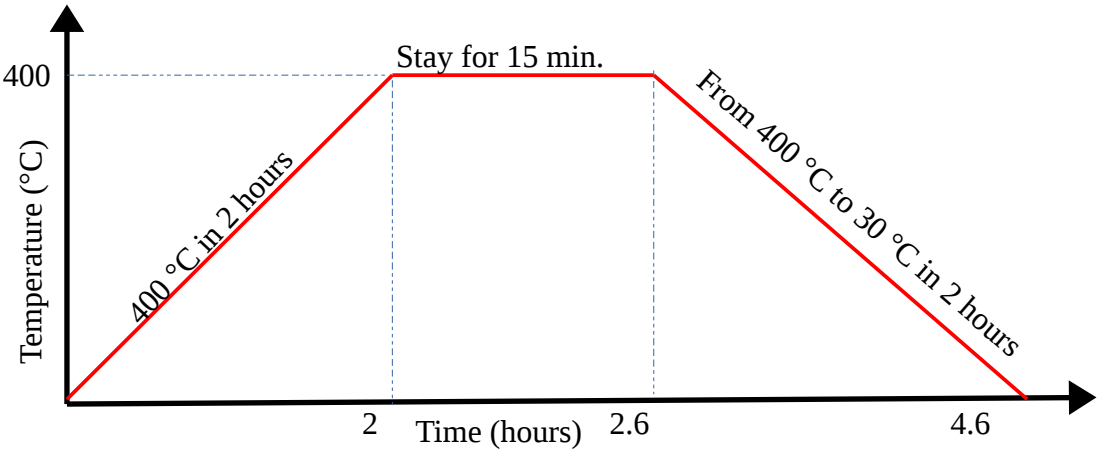

Graph 1. Optimization of sintering process for $MoS_2/BN/WS_2$ heterostructure.

Third step :

After sintering MoS_2/WS_2/h-BN powder was dispersed in the same solvent with very less concentration of 1 mg/mL. Again this solution was subjected to ultrasonication for 2 hours at room temperature at comparatively low power 150 W. In sintering process MoS_2 and WS_2 may diffuse in one another to form an in-plane heterostructure. High power sonication can break the bonds that formed during sonication and separates as an individual layer.

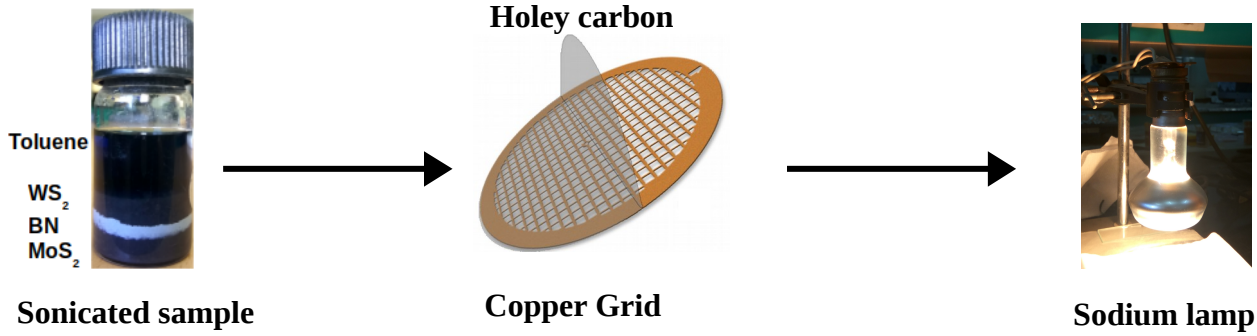

Figure 2.7 Third step of liquid exfoliaton, TEM sample preparation.

For HRTEM sample dispresed nanoparticles in the form of suspension were drop casted onto the carbon film coated copper TEM grids and dried under IR lamp.

2.4 High-Resolution Transmission Electron Microscope(HRTEM)

Transmission electron microscopy (TEM) has become one of the most powerful techniques in the fields of material science, inorganic chemistry, and nanotechnology.

In the transmission electron microscope, high energy electron beam (80-300 keV) are focused an ultra-thin specimen (~20nm) and the electrons transmit through the specimen. An image is formed when electrons interact with the sample and deflected from their original path (elastic scattering), and interfere (either constructively or destructively) with the main electron beam. The image is magnified and focused onto an imaging device, such as a CCD camera. The interactions of an electron beam with matter can be divided into two categories: elastic and inelastic interactions [6-10], which are used in the TEM and STEM to obtain structural and compositional information about the specimen. High-energy electrons with de Broglie wavelengths in the sub-angstrom range provide atomic resolution. One of the main imaging modes of a TEM is known as bright field (BF) in which only the direct, unscattered and small-angle scattered electrons are allowed to contribute to the image formation. Phase contrast is the main contrast mechanism in BF imaging and constitutes the basis for high-resolution TEM (HRTEM). Phase contrast occurs due to the difference in the phase of the electron waves inferred by interaction with the atomic potential of the atoms in the thin specimen

The most important advantage of high-resolution transmission electron microscopy (HRTEM) in materials science is its ability to provide real-space images of the local structure of thin specimens at atomic resolution (0.8 Å ICMS TITAN) as well as crystallographic and chemical information. It has been possible only by the successful construction of aberration-corrected

electron lenses in the electron microscope [11-14]. This enables direct observation of the bulk structure of complex materials and also direct imaging of local structural variations in defects, interfaces, and surfaces.

Operational modes in TEM

1.High resolution TEM images at sub-angstrom resolution

2. TEM images and electron diffraction

3. Electron Energy Loss Spectroscopy (EELS)

4. EDX- compositional analysis at nm-scale

5. High resolution STEM mode at sub-angstrom resolution

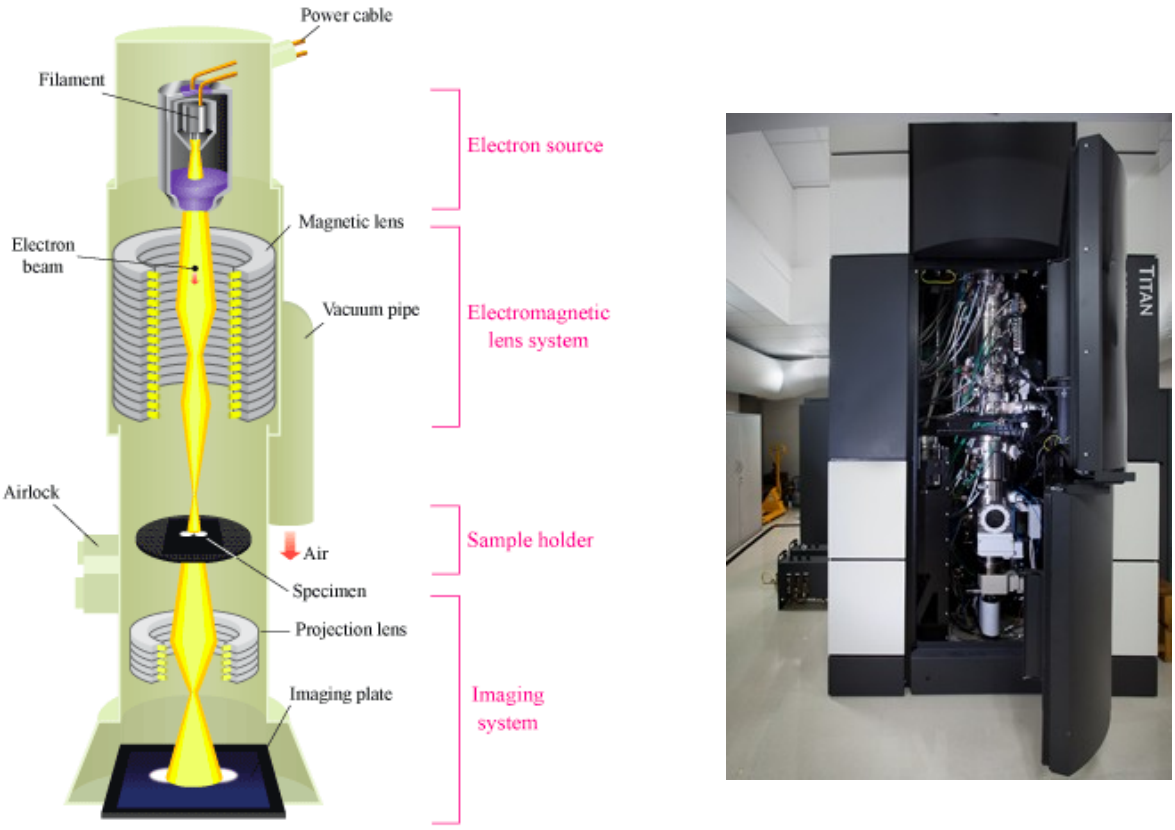

Figure2.8 Transmission Electron Microscope. (a) The basic working principle and structure of a TEM. (b) FEI TITAN3 80-300 kV used throughout this project.

Specification of TITAN 80-300 kV

FEI TITAN3 80-300 kV is one of the most powerful transmission electron microscopes in the world today. This microscope is based on double C corrector s technology (both image and probe corrector). Sub-angstrom resolution (better than 0.9 Å) is achievable both in HRTEM and STEM-Z contrast imaging. With the use of gun monochromator, now it is possible to achieve energy resolution better than 0.2 eV in electron energy loss spectroscopy (EELS). Simultaneous atom by atom imaging and spectroscopy is a very powerful tool to study and solve many of the materials challenges facing today.

2.5 Energy Dispersive X-Ray Analysis (EDX)

EDS makes use of the 'Characteristic X-rays' emitted by a solid sample bombarded with a focused beam of electrons to obtain a localized chemical analysis. Characteristic X-rays are produced when an element is bombarded with high-energy particles, which can be photons, electrons or ions (such as protons). When the incident particle strikes a bound electron (the target electron) in an atom, the target electron is ejected from the inner shell of the atom. After the electron has been ejected, the atom is left with a vacant energy level, also known as a core hole. Outer-shell electrons then fall into the inner shell, emitting quantized photons with an energy level equivalent to the energy difference between the higher and lower states.

Once we know what elements are present in our sample, we can investigate the percentage of each element by investigating the relative intensity of characteristic X-ray peaks.

The concentration of a present element is proportional to the intensity of the observed characteristic X-ray signal. Since it is difficult to measure an "absolute" intensity but by comparing measured values for two elements we can find the relative percentage of each element.

$$\frac{C_A}{C_B} = k_{AB}\frac{I_A}{I_B}$$ Clif-lorimer equation

$$C_A + C_B = 100\%$$

The convention is to used wt%.

2.6 Electron Energy Loss Spectroscopy (EELS)

Electron energy loss spectroscopy (EELS) is a techniques that measure the change in kinetic energy of electrons after interacting with the specimen. As electrons pass through a specimen, they interact with atoms of the solid. The interaction between electrons and material can be classified into two categories: eleastic and inelastic interaction [6-10]. In the eleastic interaction there is no change in energy, only momentum gets change. In the inelastic interaction there is exchange in both energy and momentum between fast moving electron and atomic constituents namely, nucleus and surrounding electrons. In EELS, the elastically scattered electrons form a peak of highest intensity known as the ‘zero loss peak’ (ZLP) and the inelastically scattered electrons form a spectrum spanning up to 2000eV accessible through the spectrometer. There are various inelastic interaction possible and we mostly concerned with two varieties, firs type is the low loss signal within few eVs from the zero loss peak which gives information on the band gap and nature of band gap (direct or indirect band gap) whereas second type, core loss spectra which provides information on the density of unoccupied states.

The spectrum till ~50eV from zero loss peak is known as electron energy loss near edge structure (EELNES) which provides information about band gap of absorbing material. Spectra beyon 50eV is known as electron energy loss extended fine structure (EELEFS) which provides information about bonding environment and coordination of material. Both

EELNES and EELEFS are same as XANES and EXAFS techniques in X-ray absorption performed in a synchrotron. In XAS mainly we get information from surface of the material but in EELS we get information from bulk. In EELS both energy and momentum transfered so we can get more deep information by momentum resolved electron energy loss spectroscopy (MR-EELS) like photonic density of state [18].

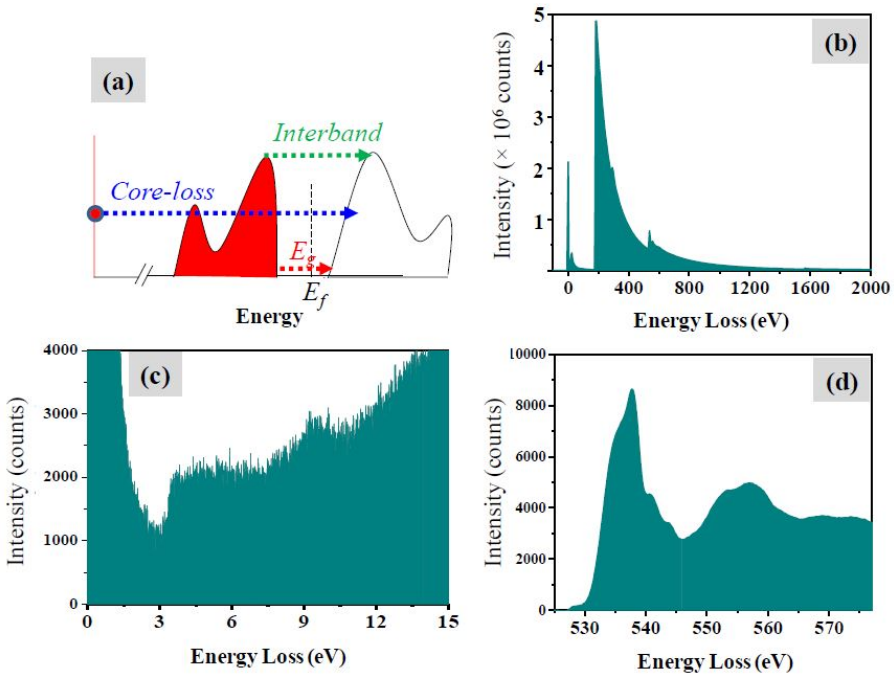

Figure 2.9 (a) Schematic energy level diagram of absorption phenomena in EELS showing various electronic transitions like band gap, interband and core-loss absorption. (b) Spectra displayed till 2000 eV for Al_2O_3. The intensity is blown up by × 350 times after 178 eV to highlight fine features. (c) EELS in the low-loss region and (d) core loss EELS for O K from ZnO.

2.7 Raman spectroscopy

When light is scattered from a molecule or crystal (by vibrating molecules), most photons are elastically scattered. The scattered photons have the same frequency and wavelength, as the incident photons. However, a small fraction of light (approximately 1 in 107 photons) is scattered at optical frequencies different from the incident photons, and usually lower than, the frequency of the incident photons. The process leading to this inelastic scatter is termed

the Raman effect. Raman scattering can occur with a change in vibrational, rotational or electronic energy of a molecule. If the scattering is not elastic, the process is called Raman scattering, if it is elesting then process called Rayleigh scattering.

2.8 Photoluminescence

Photoluminescence spectroscopy is method of probing the electronic properties like band gap et al. of materials. Light is directed onto a sample, where material absorbes light and imparts exces energy into the process called photo-excitation. There are different ways to dissipate this excess energy. One way this excess energy can be dissipated by the sample is through the emission of light, or luminescence. This Photo-excitation is called photoluminescence. Photo-excitation causes electrons within a material to move into allowed excited states. When these electrons return to their equilibrium states, the excess energy is released and may include the emission of light (a radiative process) or may not (a nonradiative process). The energy of the emitted light (photoluminescence) relates to the dierence in energy levels between the two electron states involved in the transition between the excited state and the equilibrium state. The quantity of the emitted light is related to the relative contribution of the radiative process

Bibliography:

[1] Camelia Popescu, Dr. Dongfang Yang (Ed.), InTech, DOI: 10.5772/65124.

[2] I. Paradisanos, E. Kymakis, et al., APL. 105, 041108 (2014).

[3] *C. Belouet, Applied Surface Science 96-98 (1996) 630-642.*

[4] B. Loukya et al., Journal of Crystal Growth, 329, 20-26, (2011).

[5] Badri Vishal, et al., Superlattices and Microstructures, 115, 197-203, (2018).

[6] D. B. Williams and C. B. Carter, Transmission Electron Microscopy; A Text Book for Materials Science, (Springer Science + Business Media LLC, 2009).

[7] R. F. Egerton, Electron Energy Loss Spectroscopy in the Electron Microscope, (2nd edn. Plenum, New York, 1996). [3] P.W. Hawkes and J.C. Spence, Science of Microscopy, (Springer Science + Business Media LLC, 2007).

[8] S. J. Pennycook and P. D. Nellist, Scanning Transmission Electron Microscopy (Springer Science + Business Media LLC, 2011).

[9] R. Brydson, Electron Energy Loss Spectroscopy (Garland Science, first edition, 2001).

[10] R. Brydson, Aberration Corrected Analytical Transmission Electron Microscopy, (John Wiley & Sons, Ltd., 2011).

[11] M. Haider, H. Rose, S. Uhlemann, B. Kabius, K. Urban, Nature 392, 768 (1998).

[12] N. Dellby, O. L. Krivanek, P. D. Nellist, P. E. Batson, A. R. Lupini, J. Electron Microsc. (Tokyo) 50, 177 (2001).

[13] K. W. Urban, Science **321**, 506 (2008).

[14] K. Dileep, et al., **JAP,** 119, 114309 (2016).

[15] V. Nicolosi et al., Science 340, 1226419 (2013). DOI: 10.1126/science.1226419.

[16] Researchers sew atomic lattices seamlessly together (2018, March 8) retrieved 8 March 2018 from https://phys.org/news/2018-03-atomic-lattices-seamlessly.html.

[17] Pablo Solís-Fernández, et al., Chem. Soc. Rev., 2017, 46, 4572.

Chapter III

Lateral and vertical van der Waals heterostructure of MoS_2/WS_2, MoS_2/BN and $MoS_2/BN/WS_2$ by sintering and liquid exfoliation

3.1 Optimization of experimental parameters

3.1.1 Experiments

MoS_2 bulk powder (99%, 2μm in size), WS_2 bulk powder (99%, 2μm in size) and h-BN bulk powder (98%, 1μm in size) and three different solvents (Hexane, Toluene and Methanol LR) were used in this project for exfoliation of monolayer, bilayers of h-BN and MoS_2/BN, MoS2/WS_2, MoS_2/BN/WS_2/BN van der Waal heterostructure.

There are various parameters that affect sample quality including the type of sonicator, a solvent that we use for exfoliation, sonication power, sonication time and concentration of the sample.

Effects of solvents

Solvent	**Stability (Time)**	**Sample quality in TEM**
Toluene	2 Hours	Thin few layers of h-BN, MoS_2 were found but due to high boiling point oil like contamination was found.
Methanol	10 Hours	Most of the h-BN layers were Monolayers and some multilayers.
Hexane	2 Hours	Thick h-BN layers and layers were breaking
Water	- - -	Not dissolving properly

Table 3.1 Sample quality of MoS_2/h-BN/WS_2 in different solvents.

From table 2. We can see that sample in toluene is not able to exfoliate properly. Due to the high boiling point of toluene (106°C), it is not vaporizing even after oxygen-argon plasma cleaning for 30 seconds. Plasma cleaning for higher time damages sample. In the case of hexane interaction between solvent and h-BN layers is not sufficient to keep isolate monolayers. To get monolayers interaction between solvent and h-BN layers should be greater than van der Waals interaction between h-BN layers. Methanol is low boiling point solvent (64°C), ensuring that removal of the solvent is rapid and simple so it is advantageous over

toluene and hexane. Stability of sample also very high more than 10 hours. So methanol is a better choice as a solvent.

Effect of sonication power

Table 3.2 Effect of ultrasound energy on $MoS_2/BN/WS_2$ sample quality

Sample No.	Amplitude	Power	Sample quality
Sample 1	20%	150 W	Thick particles, not exfoliated properly
Sample 2	30%	225 W	Thin crystalline layers found.
Sample 3	40%	300 W	Many thin layers but layers start breaking

From table (3) we can see that 150 W is not sufficient to exfoliate sample properly and 300 W is quite high to break the sample. So suitable ultrasound power is 225 W.

Effect of sonicaton time

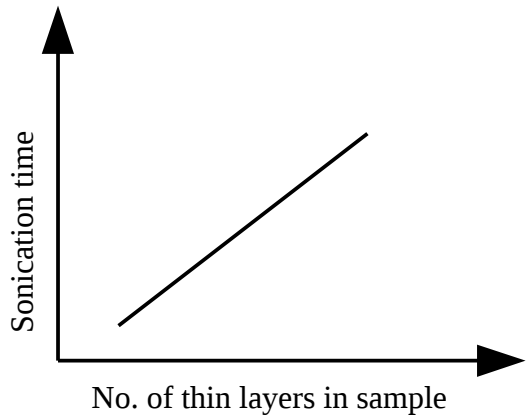

Graph 3.1 Effect of ultrasound energy on $MoS_2/BN/WS_2$ sample quality

After optimizing all the experimental parameters, finalized parameters we used.

Sample	**Amplitude**	**Power**	**Solvant**	**Time**
$MoS_2/BN/WS_2$	30%	225 W	Methanol	7 hours

Table 3.3 Final optimized parameters for ultrasonication

3.2 Vertical heterostructure

3.2.1 MoS_2 - BN vertical heterostructure

Hexagonal boron nitride (h-BN) is a wide bandgap 5.97eV insulating material [1]. H-BN promises to be an ideal substrate to improve the performance of graphene-based devices because h-BN is relatively inert and free of dangling bonds. It is found that performance of graphene devices on standard substrates like SiO_2, $Al2O_3$ is far inferior to the expected intrinsic properties of graphene [2]. Now the question comes, is h-BN playing the role of the ideal substrate in MoS2/h-BN heterostructure or it is influencing electronic properties of MoS_2.

Contradiction about MoS_2 - BN heterostructure:

(1). Theoretical calculation shows that MoS2/BN heterostructure is an indirect band gap 1.7eV [3], means h-BN has quantum quapling with MoS2 and influencing electronic properties of MoS2.

(2). Experimental PL spectra show MoS2 grown on the h-BN substrate is a direct band gap [1.86-1.89] close to free-standing MoS2. This indicates that h-BN is the ideal substrate and not influencing electronic properties of MoS2 [4-5].

(3). Again theoretical calculation shows that band gap of MoS2/h-BN heterostructure decrease as the number of h-BN layers increase. If h-BN is ideal substrate then there should not be any effect of the number of layers.[6]

(4). Theoretical calculation shows MoS2/h-BN is type-I heterostructure but there is no experimental proof [7].

There is no spectroscopy technique that can probe locally electronic properties at nano-scale. In PL spot size is used about 1 μm2. Electron Energy Loss Spectroscopy (EELS) is the only technique to probe electronic properties at nm2 scale.

To understand electronic properties of MoS2/BN at nano-scale, we have synthesized monolayer MoS2, monolayer BN, and MoS2/BN heterostructure.

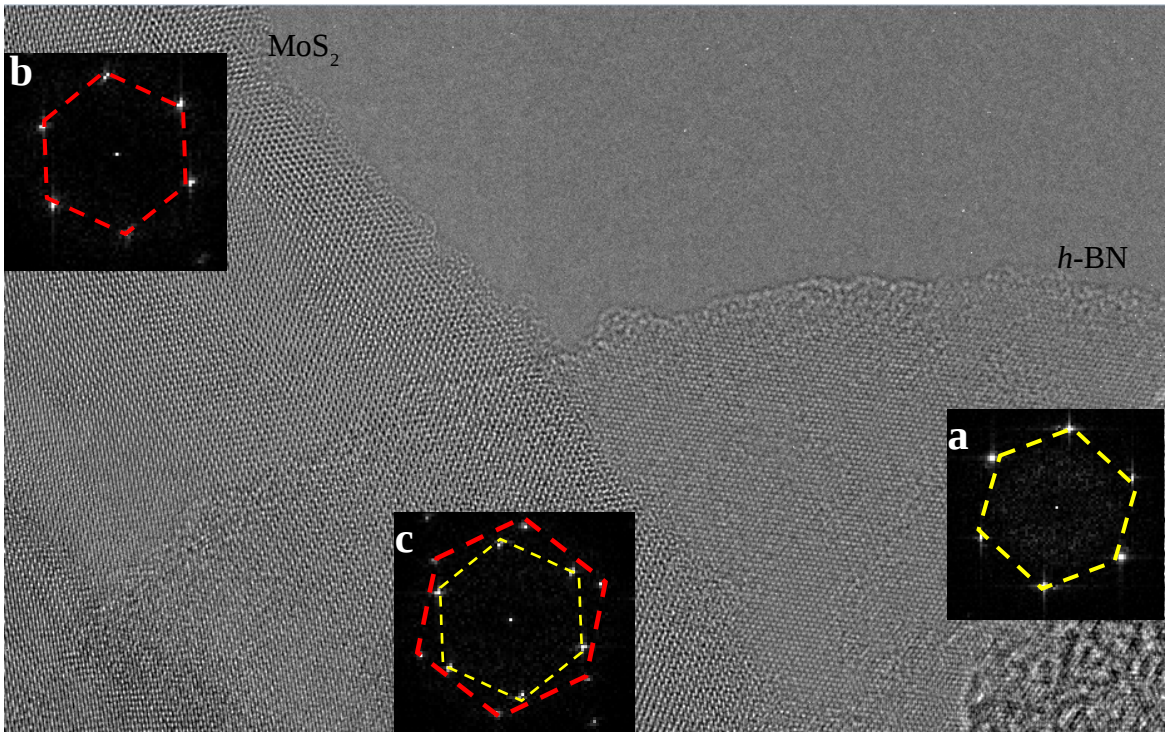

Figure 3.1 HRTEM images and FFT patterns from selected region of interest h-BN, MoS_2 and MoS_2/BN heterostructure with rotational stacking arrangement. (a) FFT pattern from h-BN region. (b) FFT pattern from MoS_2 region. (c) FFT pattern from MoS_2/h-BN overlap region.

The as grown MoS_2 /h-BN vertical heterostructure was characterized by high resolution transmission electron microscopy (HRTEM). Figure 3.1 shows monolayer MoS_2, monolayer h-BN and MoS_2/h-BN heterostructure, where the interfaces between MoS2 and h-BN can be distinguished easily by looking contrast difference in HRTEM image.

Figure 3.1 (a) shows monolayer h-BN with lattice constant 2.6Å and B-N bond length 1.5Å. FFT shows only six {11$\bar{0}$0} spots constitutes only one hexagon.

HRTEM image (b) part shows monolayer MoS_2 with lattice constant 3.3 Å and Mo-S bond length ...Å. FFT shows only six {11$\bar{0}$0} spots constitutes only one hexagon. Figure 3.1 (c) shows MoS_2/h-BN overlap region thatcan easily distinguished by the contrast difference and diffraction pattern in HRTEM image.

3.2.2 MoS_2-WS_2 Vertical heterostructure

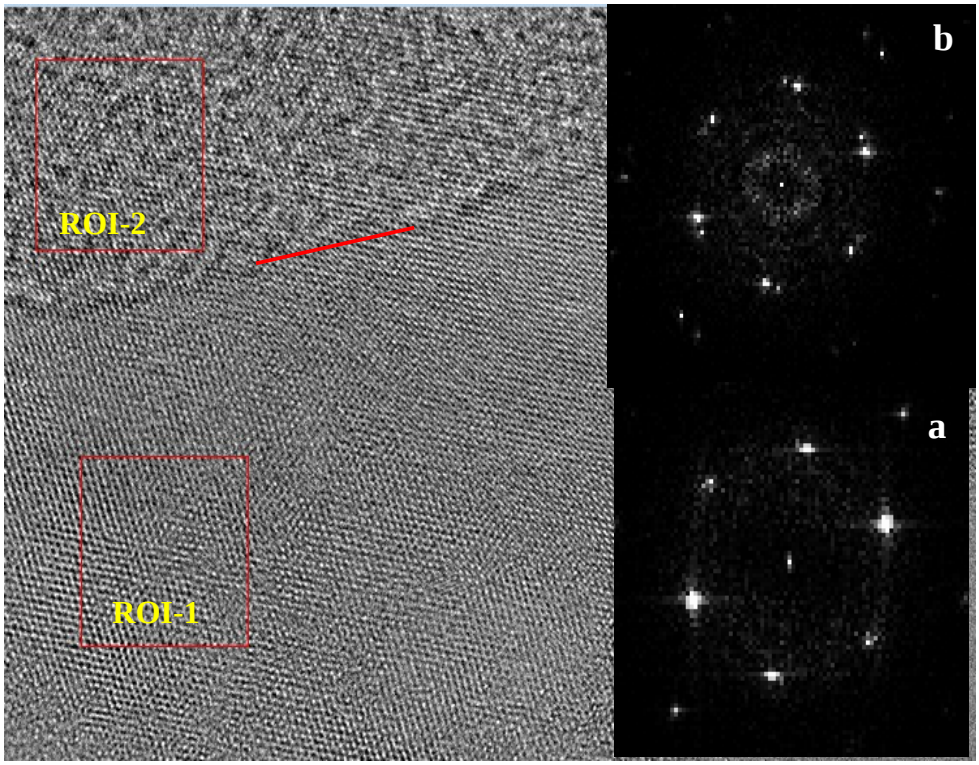

Figure 3.2 HRTEM images and FFT patterns from selected region of interest MoS_2 and MoS_2/WS_2 heterostructure. (a) FFT pattern from ROI-1 which is MoS_2 region. (b) FFT pattern from MoS_2/WS_2 heterostructure region (ROI-2).

Presence of both MoS_2 and WS_2 can be found easily by identified multiple diffraction spots in the diffraction pattern and contrast difference in HRTEM image. In figure 3.2 (a) there are 6 spots in a ring whereas in figure 3.2 (b) there are 12 spots in a ring, each 6-spot pattern represents one layer of MoS_2 and other 6 spots represent one layer of WS_2.

3.3.3 MoS_2-BN-WS_2 vertical heterostructure

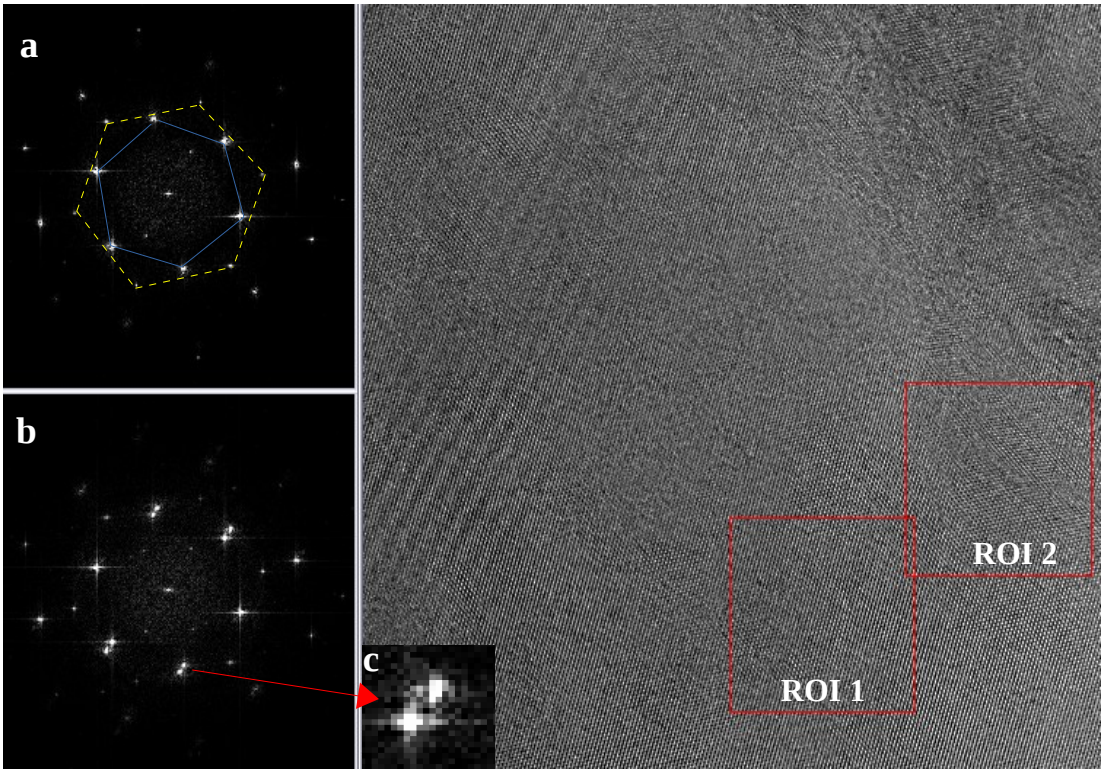

Figure 3.3 HRTEM images and FFT patterns from selected Region Of Interest(ROI) MoS_2/BN and MoS_2/BN/WS_2 heterostructure. (a) FFT pattern from MoS_2/BN region. (b) FFT pattern from MoS_2/BN/WS_2 region. (c) Magnified image to see two spots, one spot from MoS_2 and other from WS_2. pattern from MoS_2/h-BN overlap region.

Lattice parameter of *h*-BN is smaller than MoS_2 and WS_2, so reciprocal vector for h-BN will larger than MoS_2 and WS_2. In diffraction pattern, spots for h-BN appears far from central spot than MoS_2 and WS_2. From figure 3.3 (a) there are two hexagon, one is bigger hexagon and smaller hexagon. Bigger hexagon is corresponds to h-BN due to small lattice constant and smaller hexagon corresponds to MoS_2. In second diffraction pattern there are 12 spots at same distance from central spots corrosponds to two hexagon, one for MoS_2 and other for WS_2. Outer six spots are from h-BN.

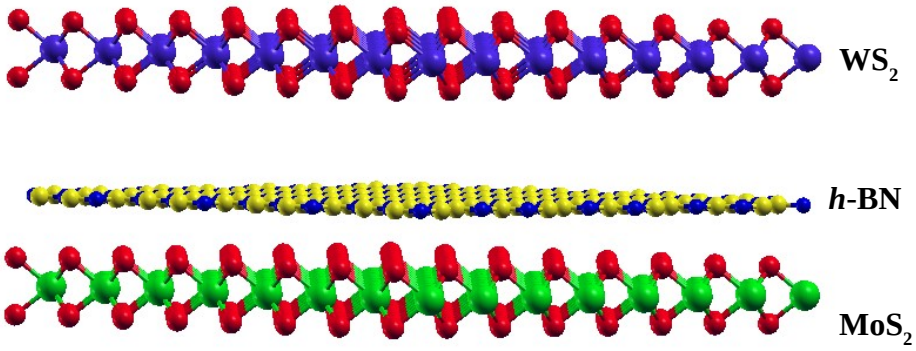

Figure 3.4 Atomic structure model for MoS_2/BN/WS_2 heterostructure to perform DFT calculation.

Band alignment in MoS_2/BN/WS_2 heterostructure

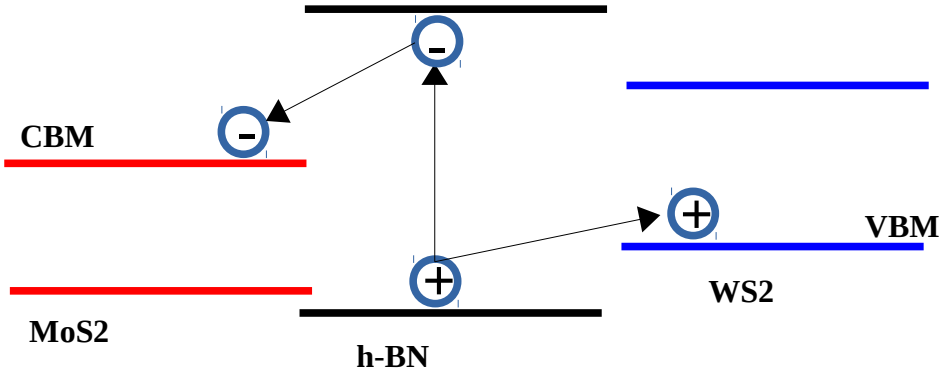

Figure 3.5 Schematic diagram of band alignment in MoS_2/h-BN/WS_2 lateral heterostructure.

MoS_2-BN and WS_2-BN are a type -I heterostructure, whereas MoS_2-WS_2 heterostructure is a type-II heterostructure.

Band alignment for MoS_2-BN-WS_2 heterostructure is shown in figure 3.5. It has properties of both type -I and type -II band alignments. When charge carriers are exited in BN layer then electron go to MoS_2 layer and holes go to WS_2 layers. This charge carrier seperation are used in so in solar cell applications. When electron and holes are excited in MoS_2, WS_2 layer, they are restricted in same layer to du to energy level. This is a properties of type-I heterostructure and used in LEDs. Another interesting properties of this system is that we can decouble MoS_2 and WS_2 layers by introducing BN layer.

3.3 Lateral heterostructure

3.3.1 MoS_2-WS2 lateral heterostructure

2D layered materials are atomically thin crystals where atoms are bonded in-plane by fully saturated covalent bonds. Due to this particular atomic structure, 2D materials are in principle free of dangling bonds in the c-direction, and they interact with their neighbouring layers via van der Waals forces, but in the plane they have dangling bonds and this gives us oppurtunity to make active these dangling bonds and stitch them to form lateral heterostructure.

Advantages of MoS2/WS2 lateral heterostructure over vertical heterostructure

(i) Lateral MoS_2-WS_2 lateral heterostructure is a direct band gap of 1.64 wheares vertical heterostructure is indirect band gap. This can improve efficience of optoelectronic devices made from [8].

(ii) lateral heterostructure has covalent bonding that gives good crystalline structure and improves optical and electronic performance of MoS_2/WS_2 heterostructure.

(iii) In vertical heterostructure band gap nature (direct or indirect) depends on many factors like interlayer distance, number of layers and surrounding of structure. However lateral heterostructure remains direct band gap only. This is an indication of robust electronic and optical properties.

(iv) Lateral MoS_2/WS_2 heterostructure forms type -II, this could avoid exciton confinement within a single layer and separates out electrons and hole in different layers. This is basic principle of solar cell application.

(v) In addition to the formation of covalent bonds, band bending occurs in lateral MoS_2/WS_2 heterostructure, which enables the concept of Schottky barrier solar cells.[9]

so lateral heterostructures are particularly promising for the spatial confinement of charged carriers, excitons and phonons within an atomically-thin layer.

MoS_2 and WS_2 are direct band gap semiconductor for 1.8-1.9eV. Both materials have same lattice constants 3.15 and 3.16 respectively. Mo and W have same oxidation states. So due to same lattice parameters covalent bonding can happen gives good crystalline structure and improves optical and electronic performance of MoS_2/WS_2 heterostructure

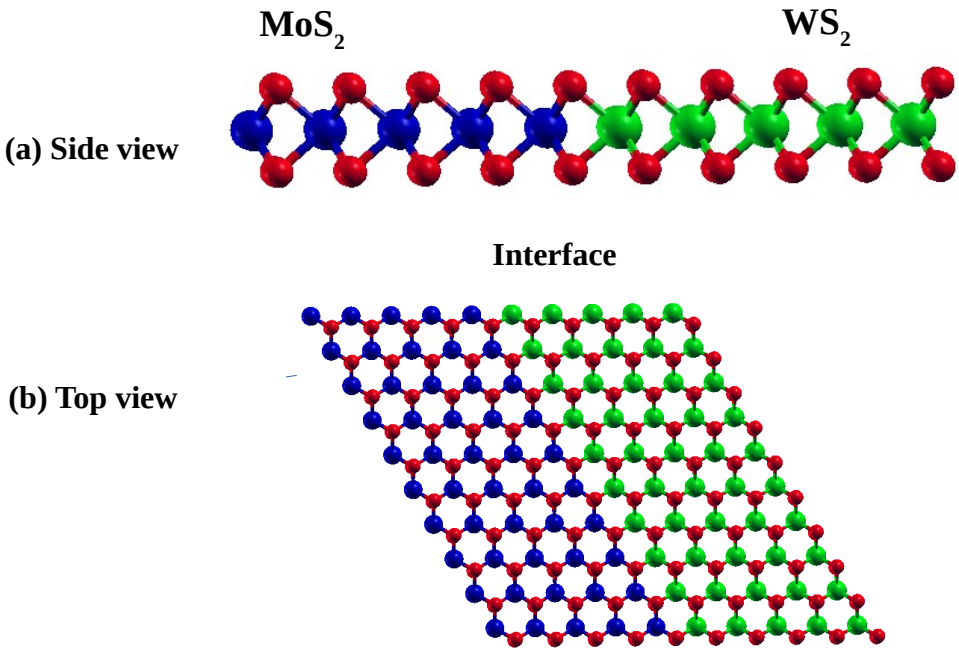

Figure 3.6 Schematic diagram of MoS_2-WS_2 heterostructure. (a) and (b) shows top and side view of heterostructure, where blue region is MoS_2 and green region WS_2.

3.3.2 MoS2/h-BN lateral heterostructure

2D layered materials are atomically thin crystals where atoms are bonded in-plane by fully saturated covalent bonds. Due to this particular atomic structure, 2D materials are in principle free of dangling bonds in the c-direction, and they interact with their neighbouring layers via van der Waals forces, but in the plane they have dangling bonds and this gives us oppurtunity to make active these dangling bonds and stitch them to form lateral heterostructure.

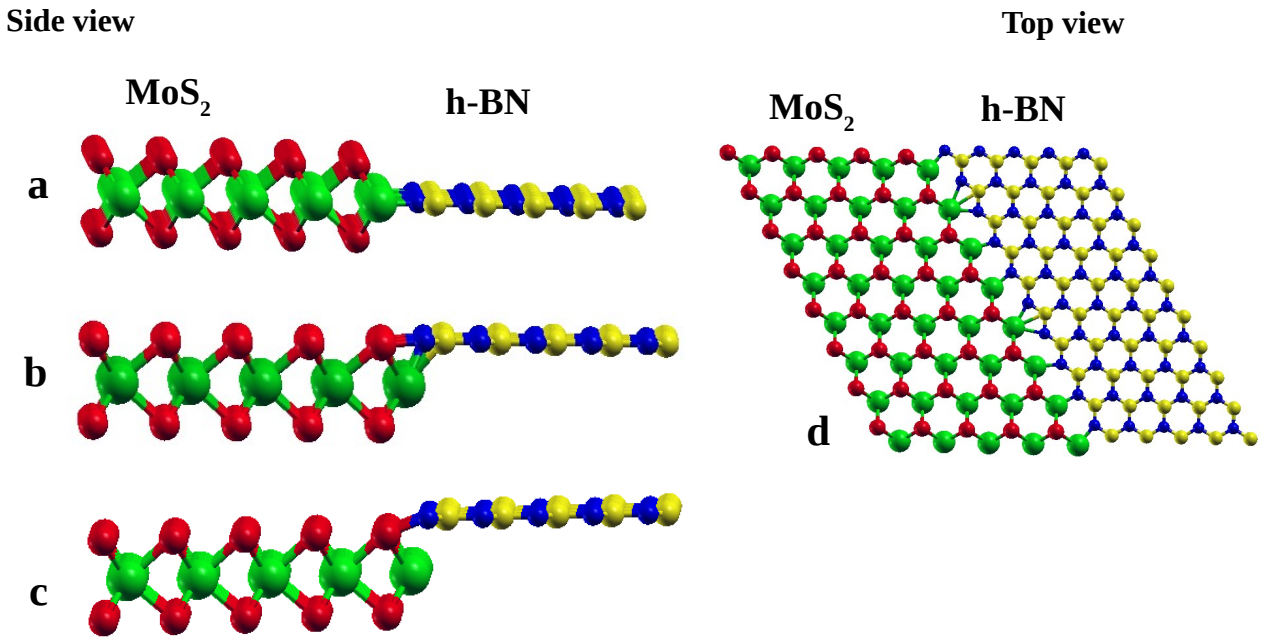

Figure 3.7 Schematic diagram of MoS_2 /h-BN lateral heterostructure. (a) MoS_2/h-BN lateral heterostructure where BN sheet prallel to Mo atomic plane and making bond with Mo atoms. (b) B and N atoms in BN sheet making bonds with S and Mo atoms respectlly. (c) BN prallel to S atomic plane and B atoms are making bond with S atom.

For MoS_2/h-BN lateral heterosturcture, there are three possibilities. In first case where BN sheet comes parallel to Mo atom it make covalent bond with Mo atom to form lateral heterostructure. Second possiblity is B atom make bond with S atom and N make bond with Mo atom. Third condition is just opposit to first condition where BN sheet parallel to S atom and make covelant bond with S atom only.

3.3.3 Lateral heterostructure of MoS_2/h-BN/WS_2

(a)Top view

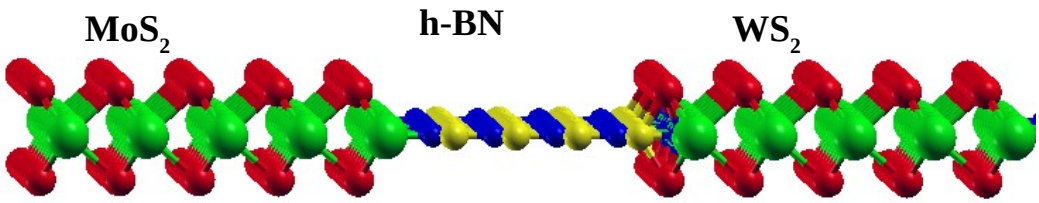

(b) Side view

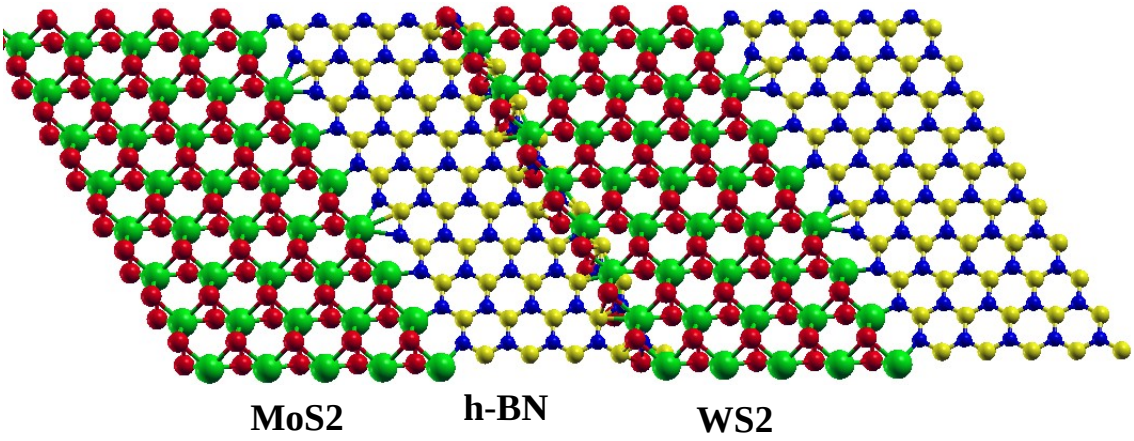

Figure 3.8 Schematic diagram of MoS_2/h-BN/WS_2 lateral heterostructure. (a) and (b) shows top and side view of heterostructure.

MoS2/BN, WS2/BN both are type-I heterostructure (Figure 3.5). When all three materials come together and make a heterostructure MoS_2/BN/WS_2 then it become type-II heterostructure. In type II heterostructure conduction band (CB) and valence band (VB) are located in different materials. Conduction band maxima (CBM) is located in WS_2 and valence band maxima (VBM) is located in MoS_2 layer. When electron and holes are execited in BN layer, holes go to WS_2 layer and electron in MoS_2 layer. This is useful for solar cell application where fast electron and holes seperation is required. In this heterostructure electrons and holes resides on different layers of semiconductor that prevent them to recombine easilly and increases their lifetime. Monolayer BN is a direct band gap

semiconductor of 4.6eV. 4.6eV energy is in UV region, so this system can be a very good UV detactor.

Band alignment in MoS2/BN/WS2 heterostructure

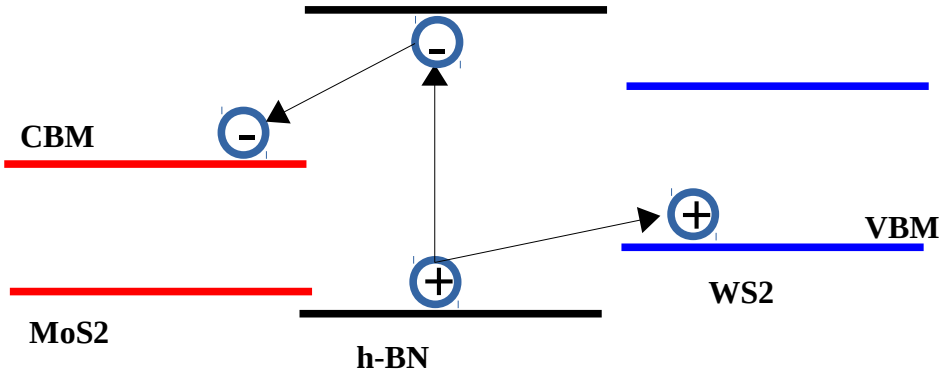

Figure 3.9 Schematic diagram of band alignment in MoS2/h-BN/WS2 lateral heterostructure.

3.4 Conclusions

In summery, we have optimized all the experimental parameters that affect synthesis of lateral and vertical van der waals heterostructure such as sonication power, sonication time, solvent and concentration of sample.

Vertical heterostructure bewteen MoS_2-WS_2, MoS_2/h-BN and MoS_2/h-BN/WS_2 have been synthesized.Theoritically we are trying to understand, the interface properties in MoS2-BN, MoS2-WS2 and MoS_2-BN-WS_2 lateral heterostructure. For MoS_2-BN lateral heterostructure we have considered three possiblities in MoS_2-BN heterostructure.

Bibliography

[1] G. Cassabois, P. Valvin, B. Gil, DOI: 10.1038/NPHOTON.2015.277.

[2] C. R. Dean, et al., Nature Nanotechnology **5**, 722–726 (2010).

[3] C. Yelgel, et al., Journal of Applied Physics 122, 065303 (2017); doi: 10.1063/1.4998522.

[4] Aiming Yan, Jairo Velasco, et al. Nano Lett. 2015, 15, 6324−6331.

[5] Lei Fu, Yangyong Sun, et al., ACS Nano 2016, 10, 2063−2070.

[6] Zongyu Huang, Chaoyu He Xiang Qi, et al., Journal of physic D, 47, 7 (2014).

[7] U.Bhat, et al., arXiv:1710.04160 (2017)

[8] Wei Wei, Ying Dai, et al., Phys. Chem. Chem. Phys., 2015, 17, 29380.

[9] M. Bernardi, M. Palummo and J. C. Grossman, Nano Lett., 2013, 13, 3664–3670.

Chapter - IV

Various stacking arrangement in h-BN bilayer and growth of w-BN thin film

4.1 Introduction

Hexagonal boron nitride (h-BN), which belongs to a hexagonal system. It has a layered structure similar to the graphene. The lattice constant (2.51Å), bond length (1.44Å) and the interlayer spacing (3.33Å) of h-BN are similar of graphene lattice constant (2.51Å), carbon-carbon bond length (1.42) and lattice spacing (3.35). Each B (1s2, 2s2, 2p1) and N(1s2,2s2,2p3) atom has s, px and py orbitals and is bonded to three neighbor atoms in the lattice, are combined by an sp2 hybridised atomic orbitals to form a strong σ bond, with the interlayers combined by weak van der Waals forces similar to graphene. Due to all these structural similar characteristics, it is sometimes referred to as 'white graphene' [1-2]. The unit cell of single-layer h-BN consists of one B and one N atom, separated by a bond length of 1.44 Å, with a lattice constant of 2.51 Å which makes it the thinnest possible insulator. In addition, h-BN is mostly inert, free of dangling bonds, making it an ideal substrate for high-quality growth of graphene and other 2D materials for electronic devices but how h-BN grows on different substrates is not fully known. We made a attempt to understand growth strategy of BN on various substrate and materials by PLD.

Substrate	**Grown allotropes of BN**
Al_2O_3 (Sapphire)	*w*-BN
MoS_2	*h*-BN
WS_2	*c*-BN + *w*-BN
ReS_2	*c*-BN + *w*-BN

Table 4.1 Growth of BN on different substrates by PLD [3-4].

The adjacent interlayers of h-BN are combined by weak van der Waals force so it can slide easily between the layers and has soft lubricating properties. Stacking arrangements are very common because energy barrier between different stackings is very small (5-26 meV).

These stacking arrangements may considerably change physical and electronic properties of layered materials.

In total, there is seven high symmetry stacking orders proposed and investigated for h-BN [Figure. 1]. These are AA (eclipsed with N over N and B over B), AA’ (eclipsed with B over N), AB (staggered with B over N),AB’ (staggered with B over B), A’B (staggered with N over N), SD(sliding N parallel to N and B parallel to B) and SD’ (sliding N and B are alternative). These can be transformed into each other by translational sliding of one of the basal planes in unit cell.

4.2 DFT calculation

To understand the effect of different stacking in h-BN bilayer on its electronic properties theoretical calculations have been performed based on density functional theory (DFT) using self-consistent plane wave pseudo potential as implemented in Quantum Espresso (QE) code [5]. The non-local vdW-DF2 functional to take into account van der Waals (vdW) interactions. The ionic core-valence electron interactions are modeled using ultra-soft pseudo-potentials [6]. Electronic exchange-correlation energy is approximated using Perdew-Burke-Ernzerhof (PBE) functional within generalized gradient approximation (GGA) [7]. The basis set consists of plane waves with the maximum kinetic energy of 500 eV. The periodic boundary conditions are applied to the rectangular unit cell with 1 B and 1 N atoms in each h-BN layer so in total there are 2B and 2N atoms in the unit cell. Additional 20 Å of vacuum is created along c-direction on top of h-BN. Integration over the Brillouin zone is performed with $12 \times 12 \times 1$ k-mesh according to the scheme proposed by Monkhorst and Pack for single-layer and all bilayer stacking h-BN. [8]. Convergence with respect to the number of k-points in the Brillouin zone and the maximum kinetic energy of plane waves was tested before calculations started. The convergence threshold of the self-consistent field is 10^{-5} eV. The optimized parameter are bond length(l)=1.455 Å, lattice parameters a=b=3.33Å and $\alpha = \beta = 90°$, $\gamma = 120°$.

We studied the electronic properties of the seven different stacking structures of h-BN bilayers.These are AA (eclipsed with N over N and B over B), AA’ (eclipsed with B over N), AB (staggered with B over N), AB’ (staggered with B over B), A’B (staggered with N over N), SD(sliding N parallel to N and B parallel to B) and SD’ (sliding N and B are alternative). The energy minima correspond to the AA’ and SD stacking in which nitrogen (boron) atoms of the top layer are located on top of boron (nitrogen) atoms of the bottom layer and sliding of upper layer by half of the lattice constant. For A’B and AB’ energy and lattice spacing in c-direction is equal. AA and AB stacking are least stable structure having large lattice spacing in c-direction.

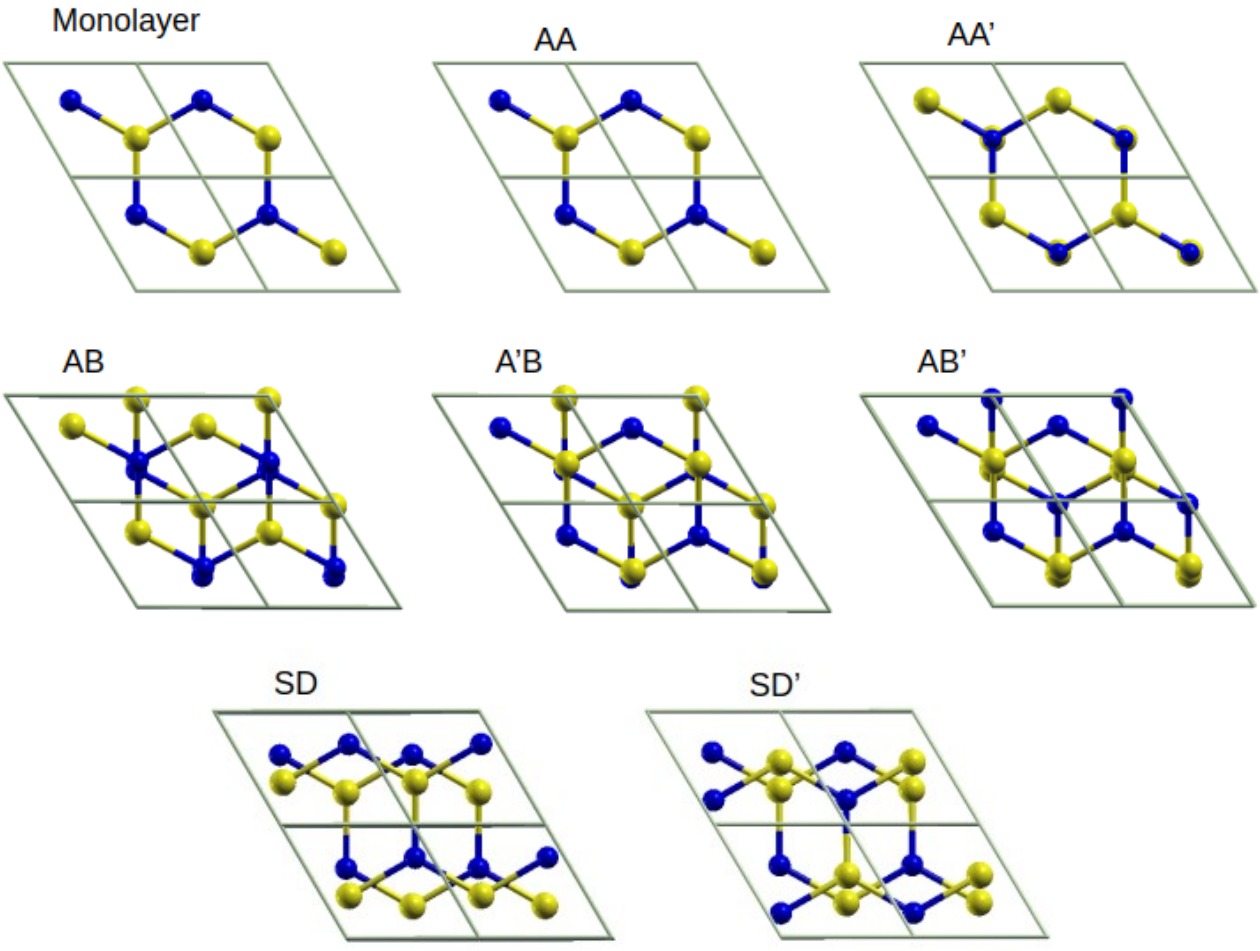

Figure 4.1 Atomic model for monolayer and various stacking in h-BN bilayer.

Stacking	Interlayer Distance (Å)	B-N bond length (Å)	ΔE_0 (meV)
AA	3.55	1.44	27
AA’	3.21	1.44	0.0
AB	3.47	1.44	25
A’B	3.14	1.44	1.5
AB’	3.14	1.44	1.5
SD	3.17	1.44	0.0
SD’	3.22	1.44	5.0

Table 4.1. Optimezed interlayer distance d_0 (Å) and the relative ground-state total energy ΔE_0 (meV with respect of most stable structure SD) for different stacking AA, AA’, AB, A’B, AB, SD and SD’.

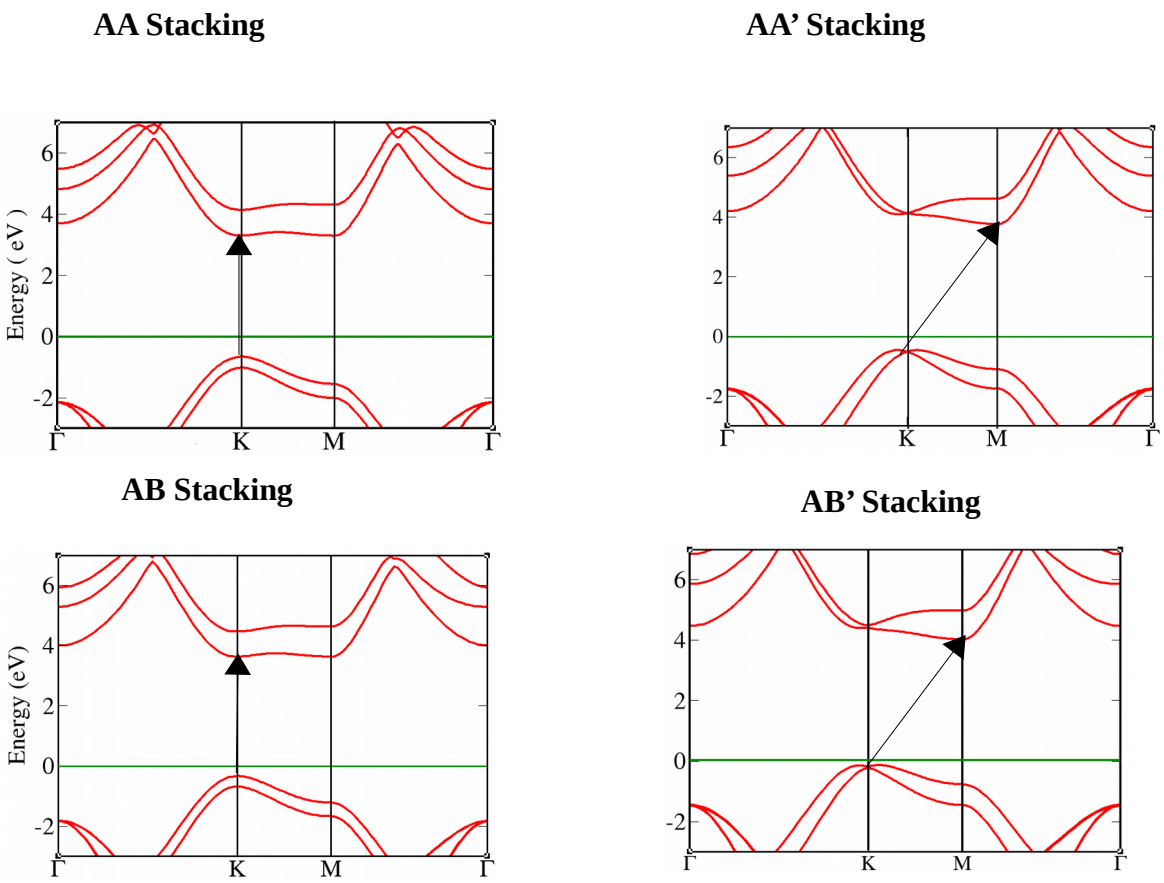

SD Stacking

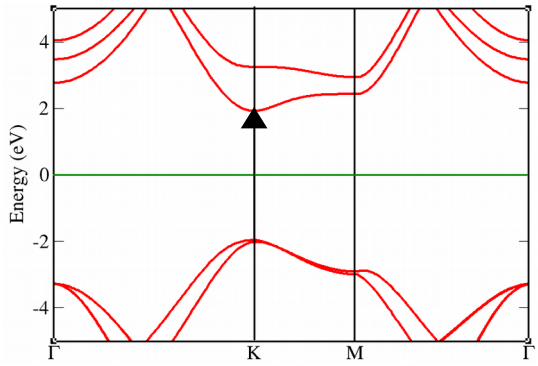

Figure 4.2 Band structure diagram for different stacking in h-BN bilayer.

From table 4.1 we can that AA' (eclipsed with B over N), and SD(sliding N parallel to N and B parallel to B) are most stable structure. Band structure calculations shows that electronic properties of h-BN is strongly influenced by different stacking. Band gap value and nature of band gap is summarized in table 4.2.

Stacking	**$K_v - K_c$ (eV)**	**K_v - M_c (eV)**	**$\Gamma_v - \Gamma_c$ (eV)**	**Nature (band gap)**
AA	**3.94**	3.95	5.8	Direct
AA'	4.65	**4.28**	5.9	Indirect
AB	**3.97**	3.97	5.8	Direct
A'B	4.57	**4.31**	5.8	Indirect
AB'				
SD	4.36	**4.29**	5.8	Indirect
SD'	**3.86**	4.37	5.9	Direct

Table 4.2 Different electronic transition energy and band gap for h-BN bilayer stacking.

From band structure calculations we can see electronic properties of h-BN is strongly influenced by different stacking, this intimate relation between stacking order and bandgap nature could serve as a fingerprint for experimental identification of possible stacking order.

Second distinct feature of band structure is the location of valence band maxima (VBM) and conduction band maxima (CBM) are found at K and M points only depending on the stacking order.

4.3 Experimental findings of different stacking in h-BN layers

4.3.1 AA’ stacking

AA’ stacking is the well-known stacking configuration for h-BN, where boron atom of top layer sits on top of nitrogen of bottom layer and vice versa. AA’ stacked multilayer layers of h-BN is shown in Figure 1a. As we can see there is exact hexagons and no other atoms appearing in the center of the hexagon. The intensities in neighboring atomic positions are

also similar to each other due to the same number of atoms giving the same sum of Z2 in the atomic columns.

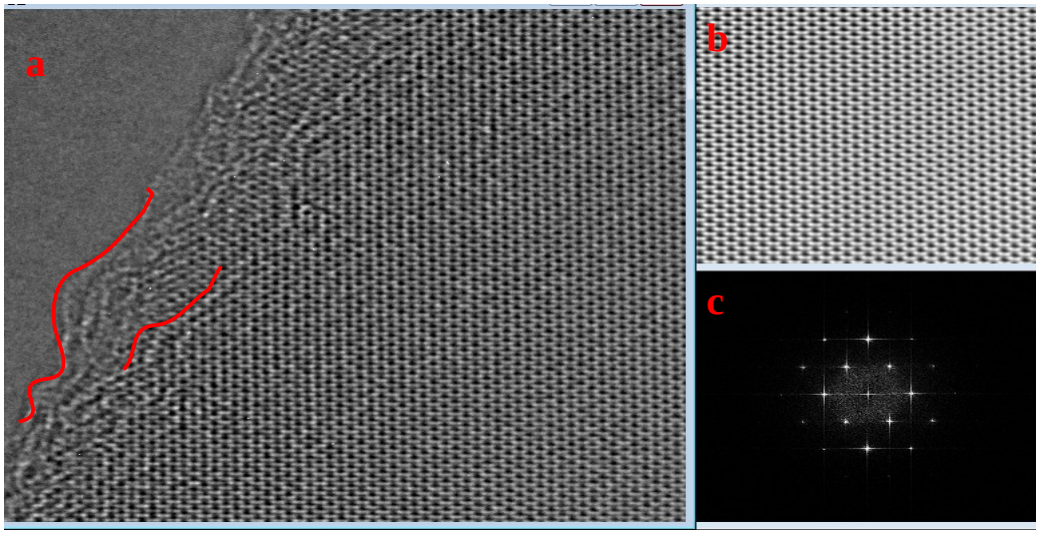

Figure 4.3 Atomic structure of h-BN layers in AA' stacking. (a) HRTEM image of h-BN layes. (b) HRTEM image is low-pass filtered HRTEM image, no artifacts are caused to remove noise in HRTEM images. The filtering is low-pass and used to remove noise and increase visibility of HRTEM images. (c) 2D fast Fourier transform (FFT) of h-BN HRTEM image. Six spots adjacent to the center are {1-100}.

Figure 1a shows the atomic structure of a bilayer h-BN sheet with the AA stacking without any rotation. The atomic structure of HRTEM image is hexagonal and having lattice constant 2.6Å and B-N bond length 1.5Å. The estimated error in lattice constants and bond length is 0.2Å which is the size of a pixel. It is interesting that no Moiré pattern is observed in the HRTEM image of the h-BN layers, shows there is no other stacking is present. Figure (1c) shows that the six $\{11\bar{0}0\}$ spots in the fast Fourier transform (FFT) pattern of the AA-stacked image constitutes only one hexagon. From figure 1a we see that the synthesized h-BN sheets are indeed 2-3 layers, as confirmed by edges. Insights into the number of layers in the BN sheets can be achieved by examining the edges. Figure 1a (red lines) shows the edge of a BN sheet with between 2 and 3 layers. Red lines in Figure 1a indicates different lines of contrast that could be due number of layers of BN.

4.3.2 AB Staking

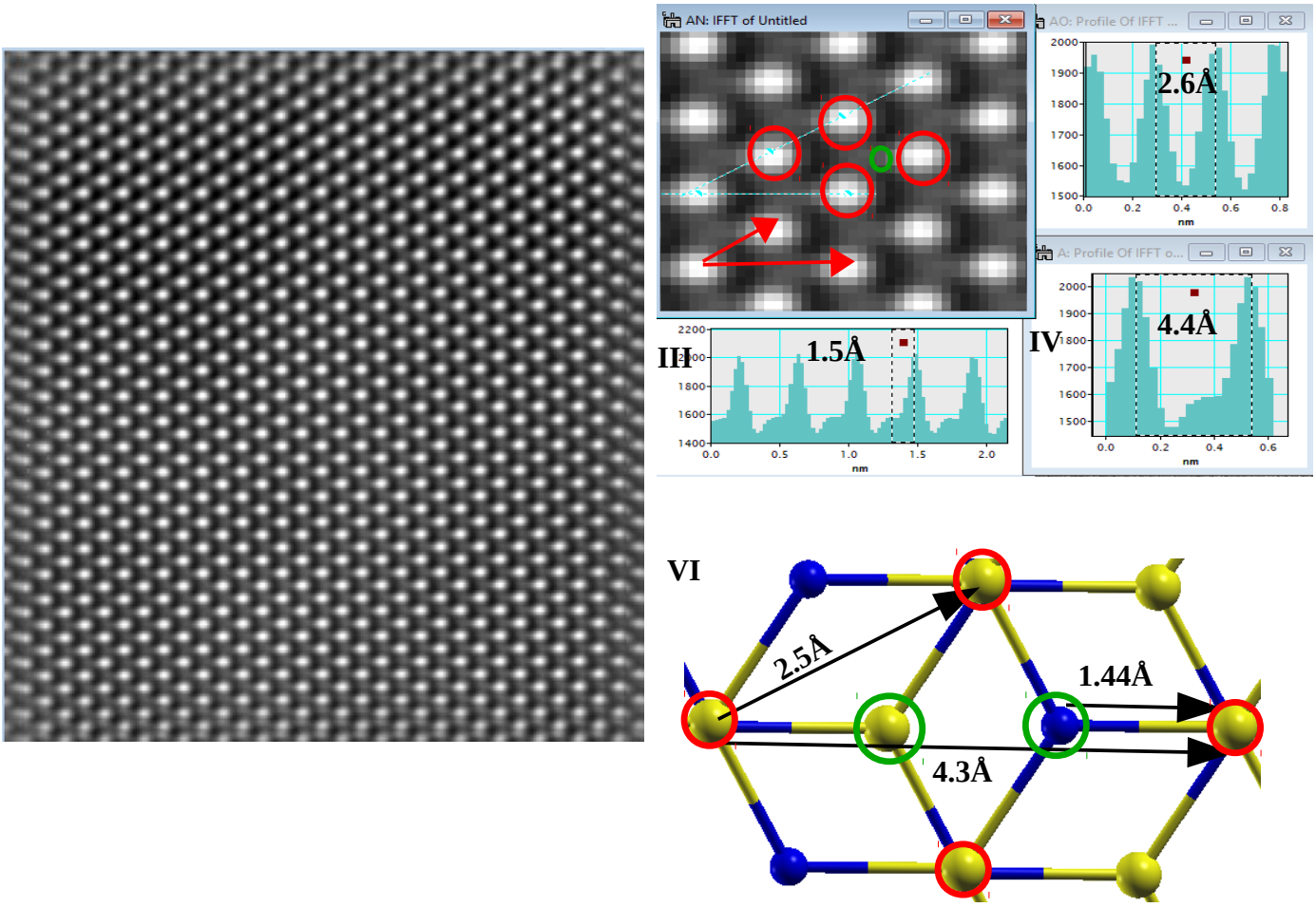

Figure 4.4 Atomic structure of h-BN layers in AB stacking and comparing with theoretical structure. (a) HRTEM image of h-BN in AB stacking. (I) Magnified HRTEM image of (a). (II) the lattice constant in direction of the small red arrow. (III) Lattice constant along the big red arrow. (IV) Atomic structure model in AB stacking showing all the lattice parameters is matching with HRTEM image.

Figure 2a shows the atomic structure of a bilayer h-BN in AB stacking without any rotational stacking arrangement. HRTEM image in AB stacking is exactly matching with atomic structure model with all lattice parameters. In AB stacking B atom of top layer overlaps with N atom of the bottom layer, so intensity in HRTEM will higher for two atomic sites (red circle) than single atomic site (green circle). There are two single atomic sites (green circle) one for B atom of the bottom layer and other for N atom of the top layer. Intensity for N atom

of the top layer is higher than B atom of the bottom layer, so only N atom of the top layer is resolving in HRTEM image due to higher Z contrast and higher phase contrast.

4.3.3 Rotational stacking arrangement with 30° rotation

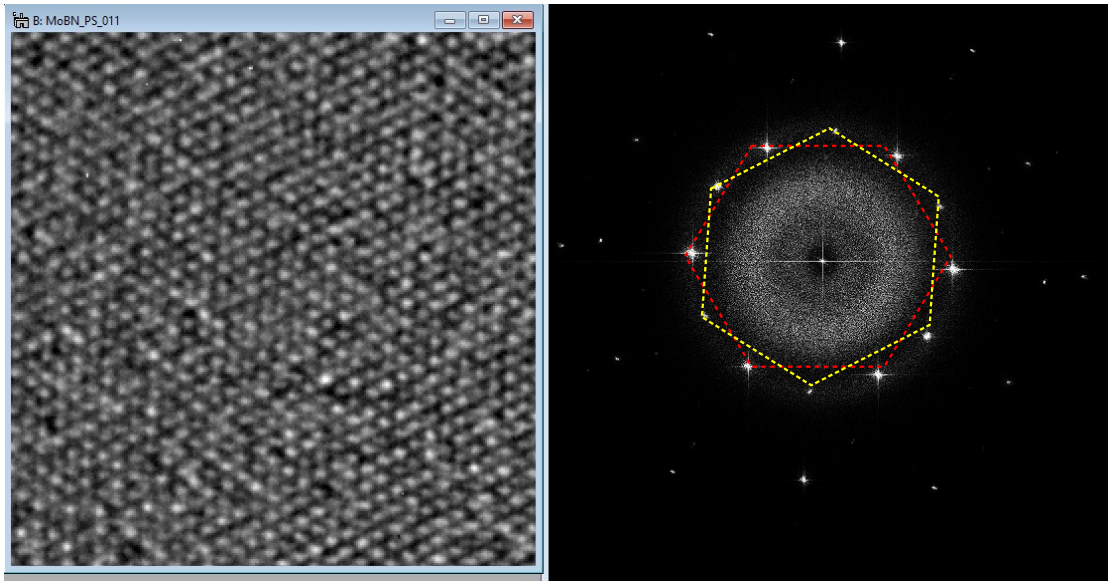

Figure 4.5 HRTEM images and FFT patterns of a bilayer h-BN sheet with 30^{o} of ratational stacking.This HRTEM image is raw and unfiltered. the twelve $\{11\bar{0}0\}$ spots constitute two hexagons that are indicated with red and yellow hexagon.

The rotational stacking in h-BN layers is easily identified by multiple diffraction spots in the diffraction pattern. Rather than having only 6 spots in each ring as in the case of single and Bernal-stacked few layer h-BN, several sets of 6 spots appear for disoriented layers (6, 12, 18 etc.) where each 6-spot pattern represents one layer. The rotation angle between the layers can be determined by measuring the angle between neighboring diffraction spots in the same ring of the diffraction pattern.

From diffraction in figure 2a, there are 12 spots in each ring rather than just 6 spots and each group of 6 spots comes from different layers. The rotation between layers is 30° as measured from neighboring spots.

4.3.4 Rotational stacking arrangements with small angle

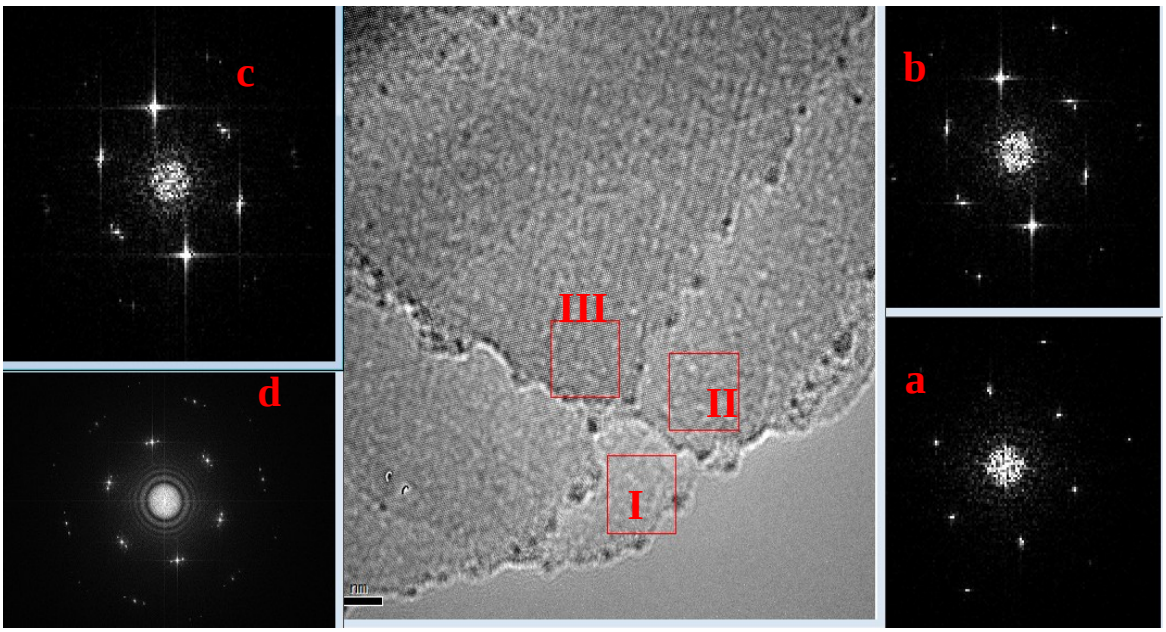

Figure 4.6 HRTEM images and FFT patterns a few layers h-BN nanosheet with three rotational stacking arrangements. (a),(b) and (c) are FFT pattern from selected region of interest I, II and III respectively. (d) is FFT pattern of whole HRTEM.

To examine the relative rotation between the h-BN layers, selected area electron diffraction (SAED) was taken three regions in figure 4. Figure 4a shows 6 diffraction spots of a hexagon. In figure (b) there are 12 spots in the diffraction pattern with a rotational angle of 3.5° between them. In figure (c) where eighteen spots constitute three hexagons. Their rotational angles are given as -3.5° and 3.5° with respect to central hexagonal spots.

These three sets of hexagonal pattern indicate that there are at least three h-BN layers, which can be seen by looking edges in HRTEM image. This symmetric rotation indicates that the orientation is not random. The number of layers can be counted by looking edges in HRTEM image.

indicating that the orientation of the *h*-BN layers is not random.

4.4 Growth of w-BN thin film by pulsed laser deposition

4.4.1 Experiment

We have grown thin films of w-BN by pulsed laser deposition on 8×8 mm^2 size ‘c’ plane sapphire substrate. The target pellet is prepared from h-BN powder obtained from Sigma Aldrich (99.9%) by first cold pressing and then sintering at 800 °C for 5 h in a vacuum chamber (~10-5 Torr). The ablation frequency used is 1 Hz during the film growth. The slow laser ablation rate allows sufficient time for kinetic relaxation of the nucleation layer to establish epitaxial relationship with the underlying substrate. This also helps in eliminating misaligned crystallites for highly lattice mismatched epitaxy. The pressure is kept constant at ~10-5 Torr throughout the growth schedule while the temperature of the growth was 400 and 800 °C for the nucleation and final growth, respectively.

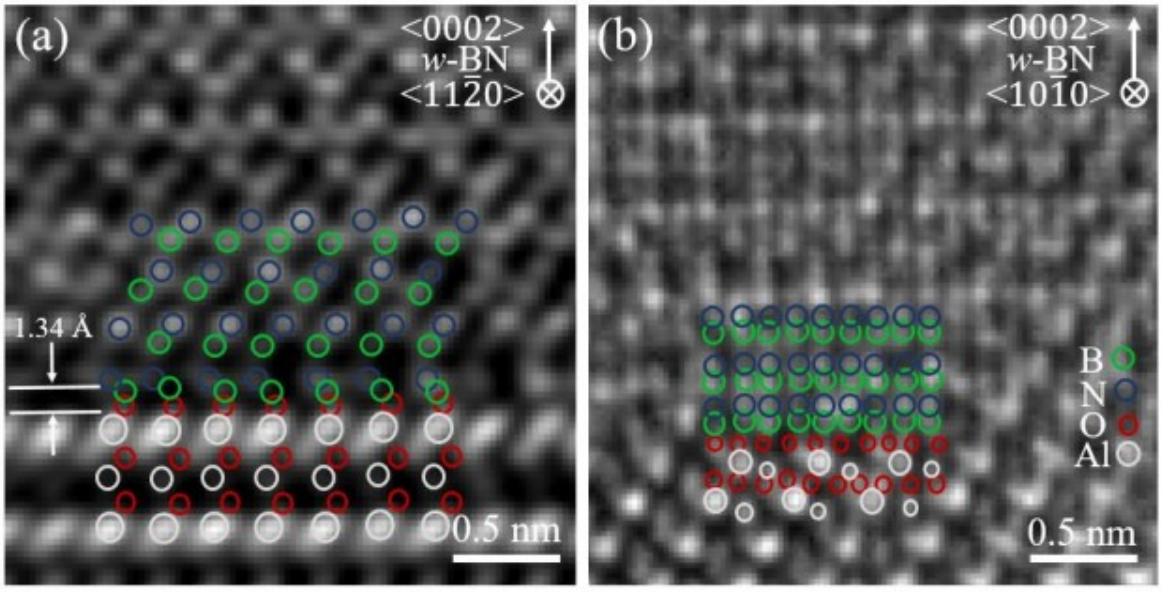

Figure 4.7 (a) & (b) HRTEM image of *w*-BN on c-plane sapphire along two different zone axes of sapphire showing atomic arrangement and registry of atoms at the film substrate interface. The inter-atomic distances are mentioned in the figure [11].

4.4.2 DFT Calculation

To understand stablization of w-BN thin film, DFT calculation were performed for both monolayer, bi-layer h-BN and staggered h-BN on O-terminated sapphire to get insights into the stability and chemical interaction through charge transfer between B and O atoms leading to structural phase transition from h-BN to w-BN. The structure of sapphire (α-Al2O3, space group $R\bar{3}c$) consists of 12 Al and 18 O atoms per unit cell with lattice parameter a = 4.758 Å, c = 12.992 Å.

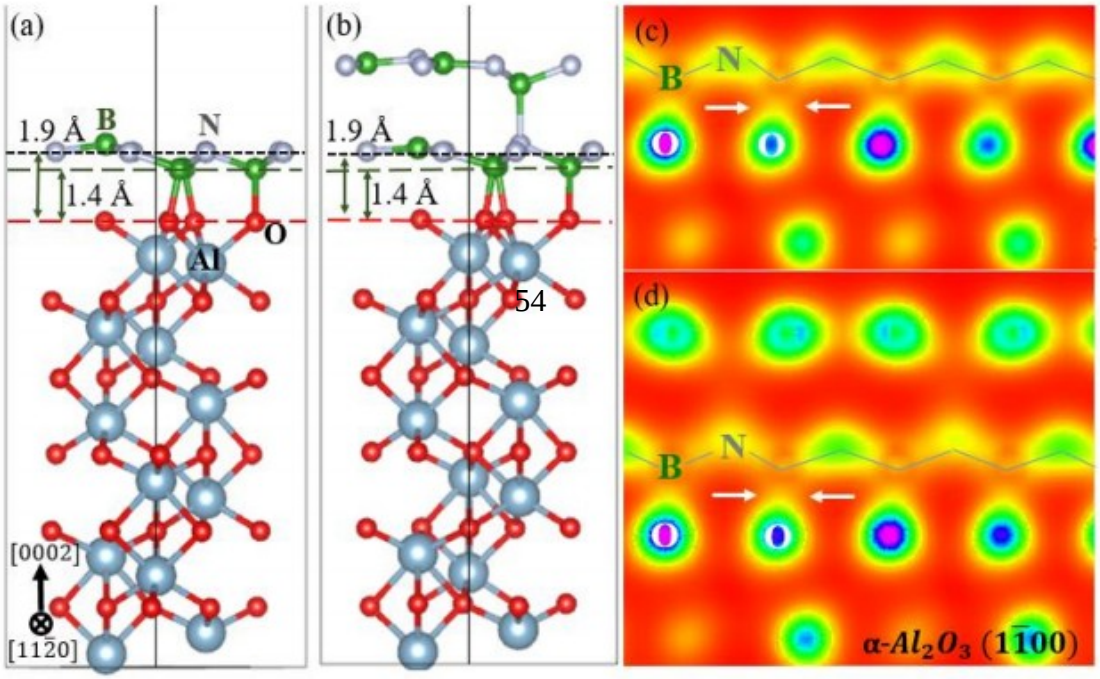

Figure 4.8 Schematic structure of monolayer (a) staggered h-BN on c-plane sapphire. The stability of staggered h-BN configuration is 210 meV/atom more compared to flat h-BN. (b) staggered bilayer h-BN showing nucleation and growth of w-BN phase along c direction. Charge density plot showing additional interaction between B and O atoms at the interface in both (c) mono and (d) bi-layer leading to staggering configuration of flat h-BN [11].

The calculation revealed that w-BN on sapphire with B-O bonding is more stable (7.76 eV/atom) than h-BN (7.55 eV/atom) for the monolayer coverage. Further calculation

shows that the staggering propagates to the bi-layer as a stable system (7.92 eV/atom) compared to bi-layer flat h-BN (7.83 eV/atom) and eventually form the wurtzite structure [Fig. 1(b)].

The valence charge density plot reveals charge transfer between O and B atoms for staggered h-BN [Fig. 1 (c) & (d)] but not for the flat h-BN. The observation by HRTEM imaging at the interface and combination of first principle calculation suggests that the selective and stronger chemical interaction between the O atoms and B atoms in h-BN for the first deposited layer initiated the structural phase transition from h-BN to w-BN and subsequently propagated along the (0001) direction.

4.5 Conclusions

In conclusion, we have grown large area epitaxial thin film of meta-stable w-BN by pulsed laser deposition on sapphire c-plane substrate. To understand stabilization of w-BN thin film we performed DFT calculation and found that interaction between O atom of sapphire and B atom of BN layer is stabilizing the meta-stable w-BN thin film. Other than w-BN, we wanted to see the influence in electronic properties of h-BN bilayer by different rotational stacking arrangement. For this, we have synthesized h-BN bilayers and multilayers in different rotational stacking arrangement and performed DFT calculation. We found that energy barrier between most stable structure and structure with rotational stacking arrangements are very less (5-25meV). From the DFT calculation, we found that bandgap nature changes from indirect to direct band gap when stacking arrangements occurs.

Bibliography

[1] Yuanyue Liu, et al. *Nano Lett.*, **2011**, *11* (8), 3113–3116.

[2] Jingang Wang, et al., RSC Adv., 2017, 7, 16801.

[3] Badri Vishal, et al., Superlattices and Microstructures, 115, 197-203, (2018).

[4] U.Bhat, et al., arXiv:1710.04160 (2017)

[5] P. Giannozzi, S.Baroni, et al., QUANTUM ESPRESSO: a modular and open-source software project for quantum simulations of materials,J. Phys. Condens. Matter, 21 (2009), 395502.

[6] D. Vanderbilt, Soft self-consistent pseudopotentials in a generalized eigenvalue formalism Phys. Rev. B, 41 (1990), p.7892.

[7] J.P. Perdew, K. Burke, M. ErnzerhofGeneralized gradient approximation made simple Phys. Rev. Lett., 77(1996).

[8] H.J. Monkhorst, J.D. PackSpecial points for Brillouin-zone integrations Phys. Rev. B, 13 (1976).

Chapter V

Conclusion and future perspectives

5.1 Conclusion

- We have optimized experimental parameters (solvent, sonication power, concentration of sample and sonication time) for van der Waals heterostructure of TMDs and BN.
- Different vertical heterostructure has been grown, MoS2/h-BN, MoS2/WS2, MoS2/BN/WS2.
- Lateral heterostructure of MoS2/WS2, MoS2/BN, MoS2/BN/WS2 have been studied.
- We studied growth of BN on Al2O3 and different TMDs (MoS2, WS2 and ReS2) and different rotational stacking arrangements in h-BN bilayer.
- Electronic structure of h-BN bilayer has been studied in various rotational stacking arrangements.
- we have grown large area epitaxial thin film of meta-stable *w*-BN by pulsed laser deposition on sapphire c-plane substrate.

5.2 Future perspectives

- We will extend our PLD growth method for vertical van der Waals heterostructure to grow a large area epitaxial thin film of the lateral heterostructure of different TMDs and BN for devices application.
- By EELS and MR-EELS we will understand interface properties of all vertical and lateral heterostructure.

Publications:

1. B. Vishal, **R. Singh**, A. Chaturvedi, Ankit Sharma, M.B. Sreedhara, R. Sahu, U. Bhat, U. Ramamurty and R. Datta, Chemically stabilized epitaxial wurtzite-BN thin film, Superlattices and Microstructures 115 (2018) 197e203.

2. U. Bhat, **R. Singh**, B. Vishal, A. Sharma, H. Sharona, R. Sahu and R. Datta, Distinct photoluminescence in multilayered van der Waals heterostructures of MoS2/WS2/ReS2 and BN, accepted in (Physica Status Solidi B: Basic Solid State Physics).